THREE DIMENSIONAL VIBRATIONAL SPECTROSCOPY AND SHOCK INITIATION OF HMX

BY

YUXIAO SUN

DISSERTATION

Submitted in partial fulfillment of the requirements
for the degree of Doctor of Philosophy in Chemistry
in the Graduate College of the
University of Illinois at Urbana-Champaign, 2016

Urbana, Illinois

Doctoral Committee:

  Professor Dana Dlott, Chair
  Professor Martin Gruebele
  Professor Ben McCall
  Professor Ken Suslick

Abstract

3D spectroscopy was employed to probe and visualize energy flows through molecules from excited parent states. Studies with IR-Raman pump probe spectroscopy show clearly that the characteristics of the vibrational relaxation pathway depend strongly upon the initial excited states. By employing 3D spectroscopy, it is possible to track and visualize relaxation pathways for an entire range of parent states, providing a better understanding of intramolecular energy transfer.

Laser driven shocks and sum frequency generation spectroscopy were used to attempt to observe the mechanisms of initiation for HMX. Those first bond breaking events are poorly understood, and much could be learned from experimental observation. Much refinement of the sample design was done, but there was still no events observed by SFG that were clearly attributable to HMX initiation. No broadening or new peaks were observed at all, and no significant loss of SFG intensity occurred besides the expected loss from the destruction of the aluminum substrate. It is possible that a more uniform and better made sample, perhaps along with significantly more laser power, could successfully observe initiation.

Flyer driven shocks and emission spectroscopy were used to determine the relative shock sensitivities of delta and beta HMX, as well as investigate the first nanoseconds after shock compression for HMX. While previous studies by the Dlott group have observed interesting phenomena in those first nanoseconds to microseconds after shock, those studies were done on beta HMX. Similar experiments were done on delta HMX, and it exhibits similar behavior initially with a very high temperature spike, though later behavior is not identical.

For my friends and family.

Table of Contents

Chapter 1: Introduction

1.1 3D Spectroscopy:

In the first section of this thesis, the energy flows within a molecule will be probed and visualized using 3D spectroscopy, where the three dimensions are pump wavelength, probe wavelength, and time. A wide variety of substituted benzenes as well as other nitrogen containing small molecules were probed and the spectra for four representative molecules will be shown and discussed. These molecules are nitromethane and acetonitrile, as well as fully deuterated versions of both. They have both been heavily studied previously,[1-6] but never with a full range of pump wavelengths. They are chosen because their comparatively simple spectra and clear vibrational relaxation pathways allow for an excellent demonstration of the power of 3D spectroscopy, easily and clearly showing the vibrational relaxation process over time, as well as how it changes upon deuteration. This technique builds upon earlier experiments which either fixed time to look at a specific moment after excitation, or fixed pump wavelength to examine the relaxation process for a specific set of parent states.

The dynamics of vibrational energy flow are extremely important for a variety of research topics such from reaction rate theories[7] to molecular electronics[8-10]. To design molecular scale devices such as thermal diodes[11] or molecular wires[8-10], vibrational energy flow must be understood to the level where it can be predicted and controlled. If building blocks for such devices could be created such that they could be combined and the result behaved in a predictable way, such devices could be far more easily modified and improved. The goal would

be to have a sufficiently strong understanding of the effects of functional groups on energy flow that systems could be modified to suit specific needs or have specific characteristics by drawing from a tool kit of functionalization options.

In the past, the Dlott group has done a great deal of work examining vibrational relaxation pathways in small molecules such as nitromethane[6], as well as within substituted benzenes. The Dlott group has in the past demonstrated this technique on a series of aryl halides[12] X-Ph (X = F, Cl, Br, I), and was able to observe ring and functional group vibrations following excitation of the symmetric ring CH stretching mode. This was followed up by a series of experiments that demonstrate energy transfer throughout the molecule can be highly dependent on the initial parent state.[13-16] These visualizations are so powerful specifically because the pathway so strongly depends on the parent excited state. If, as originally believed, [17-20] the parent states homogenize on a rapidly to give essentially identical results downstream, then naturally a scanning the whole range of parent excited states would have little value.

1.2 Laser Driven Shocks:

In the second section of the thesis, the mechanisms and processes of energetic material initiation will be probed via SFG spectroscopy, specifically looking at delta-HMX. During the shock compression of energetic materials, there are two fundamental processes taking place: initiation and ignition.[21] As a shock moves though a bulk energetic material, directly behind the shock front initiation is taking place. Initiation is the initial reaction resulting in the first bond breaking events, leading to fragmentation of the molecule and an increase in the pressure. The initiation process

2

has been estimated to be taking place on micron length scales and hundreds of picosecond time scales.[22,23] Ignition occurs as the unstable fragments of the original molecules react and futher fragment to form low energy species such as CO_2, NO, and H_2O. The energy release primarily occurs in this stage, occurring on a length and time scale of 5-500 um and $1 - 100$ ns respectively.[24]

The much longer time and length scales allow for ignition to be studied with flyer plate impacts, as covered in the next section. However, the goal here was to learn about those first bond breaking events. There are numerous theoretical studies on these events, but experimental data is sparse.[25-28] The goal of this work is to experimentally discover what the first bond breaking events and initial fragments are for explosives and explosive simulants by studying them on the same time scale as the atomistic simulations. By both directly studying initiation as well as providing experimental data to help verify and refine theoretical models, a better understanding energetic materials on the molecular scale can be attained, thus allowing for directed improvement.

To be able to study these bond breaking events experimentally, the molecules must be probed with picosecond time resolution and nanometer spatial resolution. Table top laser driven shock systems are limited to shock velocities on the order of nanometers per picosecond.[29] Thus to achieve the desired temporal resolution, the sample thickness cannot be more than nanometers thick. In the initial experiments performed, it was determined that the current technique for creating thin films was not able to form even somewhat uniform films of such thicknesses, and so much thicker films are used for the studies here, with the eventual goal of developing better sample preparation methods.

The Dlott group has done some prior work to develop the technique starting with shocks of well-ordered self-assembled monolayers adsorbed onto metal substrates. As the shock passes through the monolayer, the molecules tilt towards the surface of the metal. SFG spectroscopy was found to be able to clearly observe this effect as the shock passed through the monolayer with picosecond time resolution. The energetic material specifically being studied here, delta-HMX, will give significantly more signal even as the noncentrosymmetric molecules of delta-HMX will give an SFG signal from the bulk of the material, allowing the technique to probe the entire thickness instead of a single molecular layer.

1.3 Flyer Driven Shocks:

As stated earlier, the slower ignition event can be studied by shocks driven by impacts from thin aluminum sheets (flyer plates). This can be used to study the explosive as a material rather than a molecule. Prior work in the Dlott group has focused on the activity of fine particles of beta HMX undergoing shock. There has been considerable research on the behavior of HMX in the nanoseconds to microseconds after undergoing shock compression. There have been models put forth that involve an initial conversion of beta to delta HMX[30-32] before ignition occurs. Delta HMX is more sensitive compared to beta by most measures,[33-35] and so studying the difference between the shock compression of beta HMX and that of delta HMX could lead to some insight on whether any initial conversion step exists.

Delta HMX is not thermodynamically stable at room temperature, reverting back to beta HMX over the course of hours to days depending on temperature and humidity.[33] As such, it is

not generally used as an explosive as it cannot be stored. It is however the thermodynamically preferred polymorph at elevated temperatures, and all other polymorphs can be converted to delta by heating.[33] By depositing a layer of HMX and converting it to delta, it is possible to use flyer plate impacts to understand how the delta reacts. By then converting the sample back to beta and impacting with more flyer plates, it becomes possible to compare the two polymorphs with presumably identical surface morphology to avoid that confounding factor.

To study these polymorphs, the emission from the shocked HMX samples is collected and sent into an emission spectrometer, which allows determination of time dependent temperature and emissivity. Significant past work has been done by the Dlott group on beta HMX particles undergoing shock compression with this system. The goal of this experiment is to compare delta and beta spray coated layers to understand the role the initial polymorph plays in those first nanoseconds, as well as comparing them to previous work to understand the difference between a spray coated layer and a well packed with particles.

Furthermore, delta and beta HMX are known to have fairly different sensitivities. In general for new energetic materials, drop hammer sensitivity[36] and friction sensitivity[37] are readily measured, but shock sensitivity is more difficult. Being able to clearly determine the relative shock sensitivities of delta and beta HMX using this flyer plate apparatus would demonstrate the utility of this system for determining relative shock sensitivity, something that currently requires large scale experimental apparatus such as a gas gun.[38] Replacing it with a tabletop capable of orders of magnitude higher throughput would be immensely valuable.

1.4 References:

(1)   Deàk, J. C.; Iwaki, L. K.; Rhea, S. T.; Dlott, D. D. *J. Raman Spectrosc.* **2000**, *31*, 263.

(2)   Deàk, J. C.; Iwaki, L. K.; Dlott, D. D. *Opt. Lett.* **1997**, *22*, 1796.

(3)   Deàk, J. C.; Iwaki, L. K.; Dlott, D. D. *Chem. Phys. Lett.* **1998**, *293*, 405.

(4)   Deàk, J. C.; Iwaki, L. K.; Dlott, D. D. *The Journal of Physical Chemistry A* **1998**, *102*, 8193.

(5)   Deàk, J. C.; Iwaki, L. K.; Dlott, D. D. *J. Phys. Chem. A* **1999**, *103*, 971.

(6)   Shigeto, S.; Pang, Y.; Fang, Y.; Dlott, D. D. *J. Phys. Chem. B* **2008**, *112*, 232.

(7)   Voth, G. A.; Hochstrasser, R. M. *The Journal of Physical Chemistry* **1996**, *100*, 13034.

(8)   Segal, D.; Nitzan, A. *The Journal of Chemical Physics* **2002**, *117*, 3915.

(9)   Segal, D.; Nitzan, A.; Hänggi, P. *The Journal of Chemical Physics* **2003**, *119*, 6840.

(10)   Michael, G.; Mark, A. R.; Abraham, N. *Journal of Physics: Condensed Matter* **2007**, *19*, 103201.

(11)   Segal, D.; Nitzan, A. *The Journal of Chemical Physics* **2005**, *122*, 194704.

(12)   Pein, B. C.; Seong, N.-H.; Dlott, D. D. *The Journal of Physical Chemistry A* **2010**, *114*, 10500.

(13)   Pein, B. C.; Sun, Y.; Dlott, D. D. *J. Phys. Chem. A* **2013**, *On Line ASAP DOI: 10.1021/jp3127863*.

(14)   Pein, B. C.; Dlott, D. D. In *Ultrafast Infrared Vibrational Spectroscopy*; Fayer, M. D., Ed.; CRC Press Taylor & Francis Group: Boca Raton, FL, 2013, p 269.

(15)   Pein, B. C.; Sun, Y.; Dlott, D. D. *The Journal of Physical Chemistry B* **2013**, *117*, 10898.

(16)   Pein, B. C.; Dlott, D. D. *The Journal of Physical Chemistry A* **2014**, *118*, 965.

(17)   Laubereau, A.; Kehl, G.; Kaiser, W. *Opt. Commun.* **1974**, *11*, 74.

(18)   Laubereau, A.; Kaiser, W. *Rev. Mod. Phys.* **1978**, *50*, 607.

(19)   Graener, H.; Laubereau, A. *Chem. Phys. Lett.* **1987**, *133*, 378.

(20)   Seilmeier, A.; Kaiser, W. In *Ultrashort Laser Pulses and Applications*; Kaiser, W., Ed.; Springer Verlag: Berlin, 1988; Vol. 60, p 279.

(21)   Dlott, D. D. In *Theoretical and Computational Chemistry*; Peter, P., Jane, S. M., Eds.; Elsevier: 2003; Vol. Volume 13, p 125.

(22)   Sheffield, S. A.; Bloomquist, D. D.; Tarver, C. M. *The Journal of Chemical Physics* **1984**, *80*, 3831.

(23)   Tarver, C. M. *The Journal of Physical Chemistry A* **1997**, *101*, 4845.

(24)   Dlott, D. D. *Fast Molecular Processes in Energetic Materials*; Politzer, P.; Murray, J. S., Eds. Elsevier: New York, 2003.

(25)   Holian, B. L. *Shock Waves* **2004**, *13*, 489.

(26)   Strachan, A.; van Duin, A. C. T.; Chakraborty, D.; Dasgupta, S.; Goddard, W. A. *Physical Review Letters* **2003**, *91*, 098301.

(27)   Nomura, K.-i.; Kalia, R. K.; Nakano, A.; Vashishta, P.; van Duin, A. C. T.; Goddard, W. A. *Physical Review Letters* **2007**, *99*, 148303.

(28)   Wood, M. A.; van Duin, A. C. T.; Strachan, A. *The Journal of Physical Chemistry A* **2014**, *118*, 885.

(29)   Gahagan, K. T.; Moore, D. S.; Funk, D. J.; Rabie, R. L.; Buelow, S. J.; Nicholson, J. W. *Physical Review Letters* **2000**, *85*, 3205.

(30)   Henson, B. F.; Asay, B. W.; Smilowitz, L. B.; Dickson, P. In *AIP Conference Proceedings*; IOP INSTITUTE OF PHYSICS PUBLISHING LTD: 2002, p 1069.

(31)   Karpowicz, R. J.; Brill, T. *Aiaa Journal* **1982**, *20*, 1586.

(32)   Asay, B. W.; Henson, B. F.; Smilowitz, L. B.; Dickson, P. M. *Journal of Energetic Materials* **2003**, *21*, 223.

(33)   Cady, H. H. S., Louis C. *LAMS* **1962**, *LAMS-2652*.

(34)   Herrmann, M.; Engel, W.; Eisenreich, N. *Propellants, Explosives, Pyrotechnics* **1992**, *17*, 190.

(35)   Peterson, P. D.; Lee, K. Y.; Moore, D. S.; Scharff, R. J.; Avilucea, G. R. *AIP Conference Proceedings* **2007**, *955*, 987.

(36)   Simpson, L. R.; Foltz, M. F. *LLNL small-scale drop-hammer impact sensitivity test*, Lawrence Livermore National Lab., CA (United States), 1995.

(37)   Simpson, L. R.; Foltz, M. F. *LLNL Small-Scale Friction Sensitivity (BAM) Test*, Lawrence Livermore National Lab., CA (United States), 1996.

(38)   Mitchell, A.; Nellis, W. *Review of scientific instruments* **1981**, *52*, 347.

Chapter 2: Experimental

2.1 A System for 3D Spectroscopy:

A diagram of the laser system for the 3D spectroscopy experiments can be seen in Figure 2.1. The 3D spectroscopy experiments start with an oscillator (Model TS Ti:Sapphire kit laser, Kapteyn-Murnane Laboratories L.L.C.). The Ti:Sapphire oscillator rod is pumped by a continuous-wave visible laser (Millennia eV, Spectra-Physics) outputting 4.5 Watts centered at 532 nm. The oscillator produces pulses of length ~100 fs with a per pulse energy of ~5 nJ at a rate of 80 MHz. These pulses are approximately Gaussian with a center of 800nm and a FWHM of 40 nm.

These pulses are fed into a chirped pulse amplifier (CPA) (Quantronix Titan-I). To prevent damage to the gain medium, the CPA first stretches the pulse to ~100 ps, then amplifies the pulse energies to ~4 mJ via a regerative amplifier followed by a multipass amplifier. A compressor then reverses the chirp from the stretcher. For this experiment, the compressor recompresses the pulses to ~0.9 ps.

The beam is then split and half is sent into a doubling crystal, giving 0.9 mJ 400nm pulses. This is then split again and sent into a pair of optical parametric amplifiers (OPA) (Light Conversion, Traveling-wave Optical Parametric Amplifier of Superfluorescence (TOPAS)). These operate via three photon parametric interactions, where the initial 400nm photons are split into two photons, conserving total energy. These two types of photons, called signal and idler, then interact with the majority of the incoming beam and are amplified. The signal/idler wavelength can be tuned, thus providing a tunable beam source.

For this experiment, one OPA is used to tune the idler from 0.95um to 1.2um with pulse energy of 15-20uJ, and the other is kept fixed at a signal wavelength of 532 nm with pulse energy of 50 uJ. The former is then mixed with the other half of the 800 nm beam from the CPA to give 2.4 - 5 um pulses via DFG, and this is cleaned up and acts as the pump pulse for the experiment. The latter is simply cleaned up and sent through a delay line and then to the sample, and acts as the probe pulse for the experiment.

Both beams are focused down to a 60um spot size onto a liquid jet formed by a 60um stainless steel capillary. A liquid jet is used as alterative systems require windows that could potentially generate fluorescence and other nonlinear signals.[2-4] This liquid jet is driven by a Hewlett Packard Series II 1090 liquid chromatography pump, which uses a dual syringe pump to minimize pressure fluctuations over the pump cycle. Any fluctuations would lead to fluctuations in Raman signal, which would be problematic. The scattered raman signal is then sent though a Kaiser optical spectrograph, and imaged onto a CCD (Princeton Instruments 1340x100 liquid nitrogen cooled multichannel CCD detector). Experiments were carried with 2 second integrations for each spectrum at each delay, with a computer controlled system to automatically shift the pump wavelength and probe delay as needed.

2.2 A System for Laser Driven Shocks:

A diagram of the laser system for laser driven shock experiments can be seen in Figure 2.2. The system uses an identical oscillator and CPA system, but the compressor in the CPA is set to compress the beams down to ~130 fs FWHM. The system also has a beam splitter which diverts 40% of the beam after the amplifier and before the compressor to an auxiliary compressor (Clark-

MXR, Inc.), which is set to instead compress the beam to 10 ps FWHM for a longer sustained shock. This pump beam is then sent through a delay line and is focused down to 150 um at the back of the sample. Originally, a diffusive beam shaper (TH-033-X-Y-A, Holo/Or) was used to form a flat top profile for the pump beam as seen in FIGURE,[5] however later experiments removed this optic to get higher peak intensities.

The remainder of the beam is sent through the compressor of the CPA as normal, and then is split 85:15, with the majority going into an OPA, same model as above. The signal and idler from the OPA are mixed together with the DFG product used as the tunable broad band IR pulse for SFG. The pulse was tunable between 2.5 um and 12um, with energy ranging from 10 uJ to 30 uJ. The bandwidth was ~200 cm^{-1} FWHM, and duration was ~250 fs. The remaining 15% of the beam is sent through an etalon to provide the narrowband visible pulse, with a spectral width of 10 cm^{-1}.

Both beams are focused down to 125 um at the sample and temporally overlapped to give an SFG signal, which is then collected with a 500is Chromex spectrograph and an Andor DU420BV CCD camera. As the shock experiments destroy the sample after each shot, the sample is shifted by 1 mm after each shot going row by row. Approximately 900 shots are averaged to give a single delay spectrum.

2.3 Sample Preparation for Laser Driven Shocks

A diagram of the sample for laser driven shocks can be seen in Figure 2.3. 1nm of chrome and 300 nm of aluminum are deposited on a 2" x 2" x 1/16" piece of borosilicate glass. On this is sprayed enough HMX to form a layer of average thickness 1 micron using an airbrush from a

solution of 50 mM HMX in acetone. While the spraying takes place, the glass substrate is heated to 35-40 C to speed up acetone evaporation. After spray coating, a PMMA shock confinement layer ~5 um thick is spin coated onto the sample from a 20% solution in chloroform. The PMMA cures essentially immediately, and the sample can be used. Due to the gradual conversion of delta HMX to beta HMX at room temperature, the samples could not be produced in advance and needed to be made the day of. The tests that lead to all of these specific factors are covered in section 4.3.

2.4 A System for Flyer Driven Shocks on HMX:

The experimental setup can be seen in Figure 2.4. Thin aluminum foils (flyer plates) are launched in a vacuum via laser, which then impact spray coated layers of HMX or control material. A photon Doppler velocimeter (PDV) system is used to determine flyer plate velocities and HMX motion after impact, and an emission spectrometer is used to collect shock-induced emission.

The flyer plate apparatus, PDV system, and emission spectrograph have been discussed previously,[6-8] and will not be covered in detail here. Homogenous top hat laser pulses with duration 20ns were used to launch 500 um diameter 50um thick aluminum flyer plates across a 375 um gap, giving shock durations of 10ns. Laser fluences of up to 500 J cm^{-2} were possible, and flyer plate velocity was changed by varying the laser fluence. The laser fluence-flyer velocity relationship was determined via PDV using spots with no sample, as the sample was essentially opaque to the PDV beam. Flyer launches are highly reproducible (± <1%),[9] and thus these should be representative of the actual impact speeds at the sample.

The emission spectrograph samples the central 50um of the impact, and covers the wavelength range 442-822 nm. The output is then binned using a log(time) algorithm. While PDV could not determine the precise moment of impact with the sample, it could detect the moment the shock front exited the HMX into the glass. For binning purposes, we define this moment as 10^{-8} s.

2.5 Sample Preparation for Flyer Driven Shocks:

A 3" × 3" × 1/4" mm glass window was used as a base for HMX spray coated from an 8ml solution of 50mM HMX in acetone using an airbrush. A stainless steel mask was used to spray the HMX in a pattern of 150 3mm diameter circles to avoid any possibility of shots affecting adjacent targets, and 37 additional circles on the glass were left empty for flyer plate velocity test shots to establish the laser fluence-flyer velocity relationship. The average thickness of the HMX within the circles was 10um. While the HMX did not appear perfectly smooth, it appeared to be fairly homogenous on the observation length scale (50 um). At each velocity, typically 12-13 emission transients were acquired.

As a control, oxalic acid was used due to its fairly similar density (1.65 g/cm^3 vs 1.91 g/cm^3 for HMX) and elemental composition. An equal mass of oxalic acid was sprayed onto glass samples in the same pattern and the emission transients were used as a baseline to determine how much of the emission results from the HMX rather than the flyer or glass.

Previous studies have shown that the HMX deposited from spray coating is primarily the delta polymorph.[10] However, studies have also shown that sensitivity can vary significantly based on small amounts of the other polymorphs.[11] Heating converts all other polymorphs to delta,[9,11,12] as such, the spray coated HMX layer is baked at 200° C for 30 minutes to remove any traces of other polymorphs before running the experiment. Based on literature kinetics values,[13-15] this should be easily sufficient, and IR was used to confirm this. For experiments involving beta HMX, the spray coated layers were exposed to acetone vapors at room temperature[11] over the course of four hours, with the time determined initially by observing the IR spectrum until conversion appeared complete. Figure 2.5 shows IR spectra for the spray coated layers of the two polymorphs, with dashed lines indicating significant peak shifts.

While systems such as the drop hammer can use microphones to determine whether initiation has occurred,[15] the situation is somewhat more complex for flyer plates. The flyer plate itself creates significant emission upon impact as does the glass, and there is also significant possibility of any organic material being impacted to emit with sufficiently high flyer velocity. As such, control samples were also made using oxalic acid, which has density comparable to HMX (1.65 g/cm^3). Samples with oxalic acid were made in precisely the same fashion as the HMX, with identical amounts sprayed on. The samples were used without any further treatment after spray coating.

2.6 References:

(1)   Sun, Y.; Pein, B. C.; Dlott, D. D. *The Journal of Physical Chemistry B* **2013**, *117*, 15444.

(2)   Chen, S.; Hong, X.; Hill, J. R.; Dlott, D. D. *The Journal of Physical Chemistry* **1995**, *99*, 4525.

(3)   Chen, S.; Lee, I. Y. S.; Tolbert, W. A.; Wen, X.; Dlott, D. D. *The Journal of Physical Chemistry* **1992**, *96*, 7178.

(4)   Hong, X.; Chen, S.; Dlott, D. D. *The Journal of Physical Chemistry* **1995**, *99*, 9102.

(5)   Berg, C.; Lagutchev, A.; Fu, Y.; Dlott, D. *AIP Conference Proceedings* **2012**, *1426*, 1573.

(6)   Peterson, P. D.; Lee, K. Y.; Moore, D. S.; Scharff, R. J.; Avilucea, G. R. *AIP Conference Proceedings* **2007**, *955*, 987.

(7)   Karpowicz, R. J.; Brill, T. *Aiaa Journal* **1982**, *20*, 1586.

(8)   Henson, B. F.; Asay, B. W.; Smilowitz, L. B.; Dickson, P. In *AIP Conference Proceedings*; IOP INSTITUTE OF PHYSICS PUBLISHING LTD: 2002, p 1069.

(9)   Banishev, A. A.; Shaw, W. L.; Bassett, W. P.; Dlott, D. D. *Journal of Dynamic Behavior of Materials* **2016**, *2*, 194.

(10)   Brand, H. V.; Rabie, R. L.; Funk, D. J.; Diaz-Acosta, I.; Pulay, P.; Lippert, T. K. *The Journal of Physical Chemistry B* **2002**, *106*, 10594.

(11)   Cady, H. H. S., Louis C. *LAMS* **1962**, *LAMS-2652*.

(12)   Herrmann, M.; Engel, W.; Eisenreich, N. *Propellants, Explosives, Pyrotechnics* **1992**, *17*, 190.

(13)   Weese, R. K.; Burnham, A. K. *Propellants, Explosives, Pyrotechnics* **2005**, *30*, 344.

(14)   Goetz, F.; Brill, T. B.; Ferraro, J. R. *The Journal of Physical Chemistry* **1978**, *82*, 1912.

(15)   Simpson, L. R.; Foltz, M. F. *LLNL small-scale drop-hammer impact sensitivity test*, Lawrence Livermore National Lab., CA (United States), 1995.
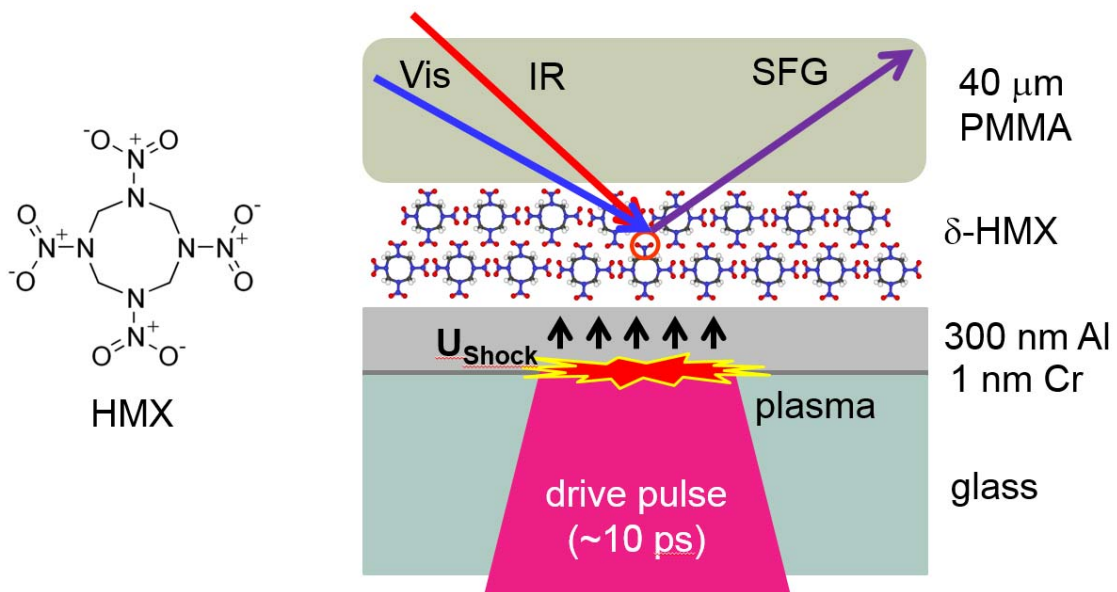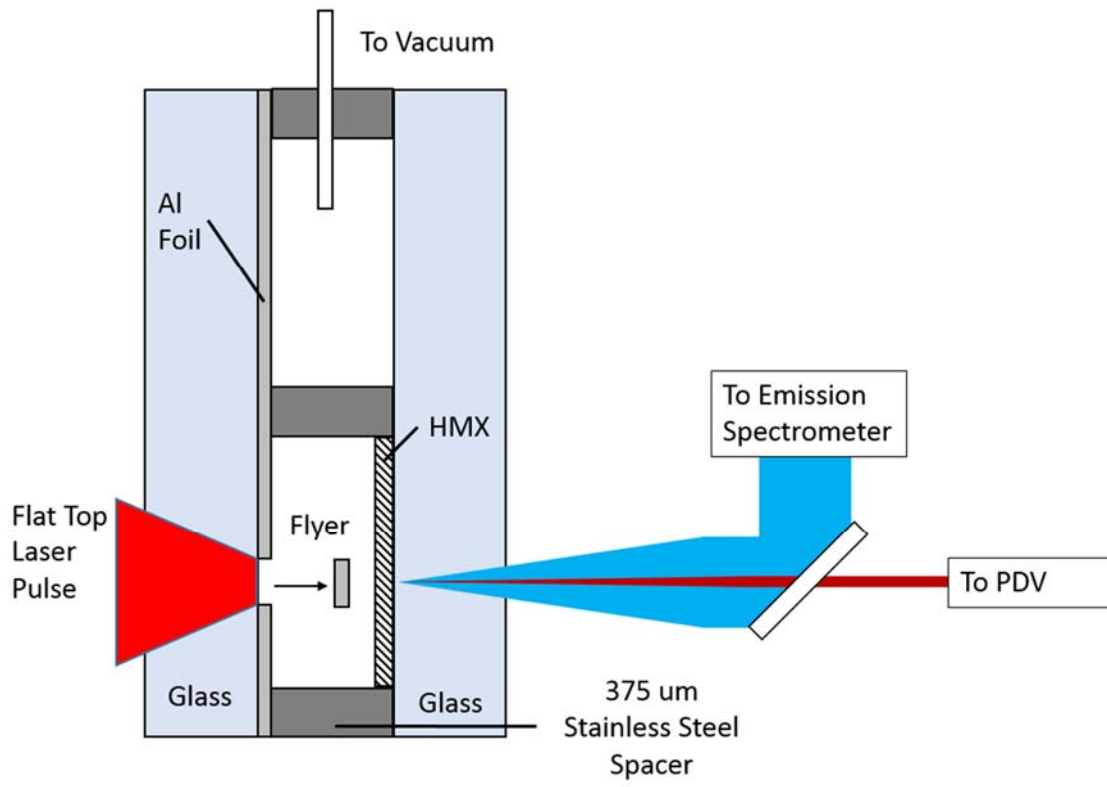
2.7 Figures:
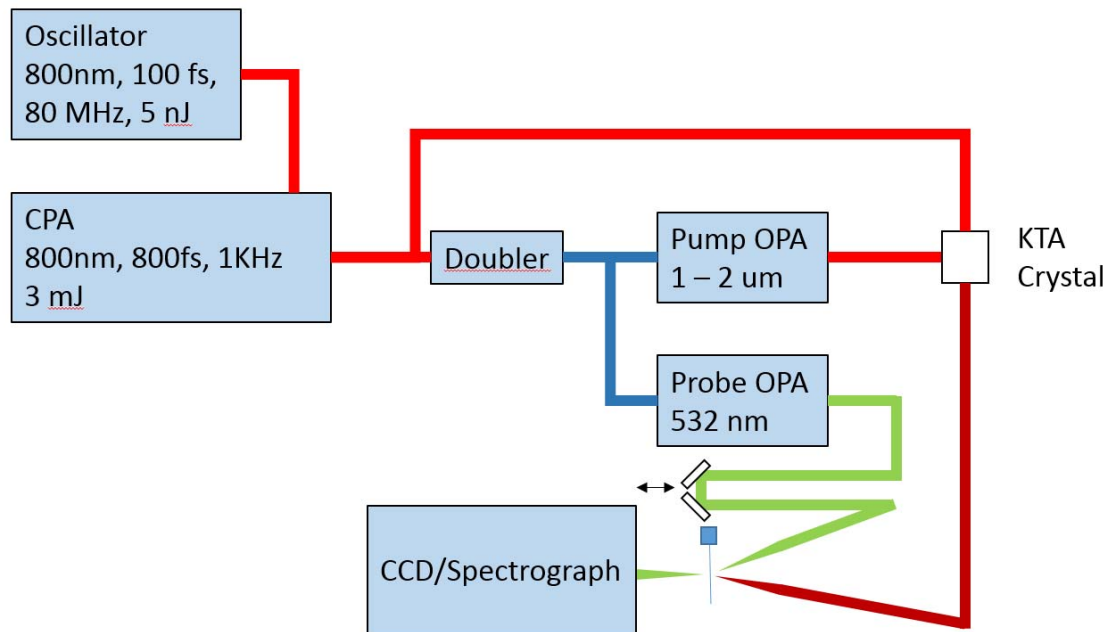
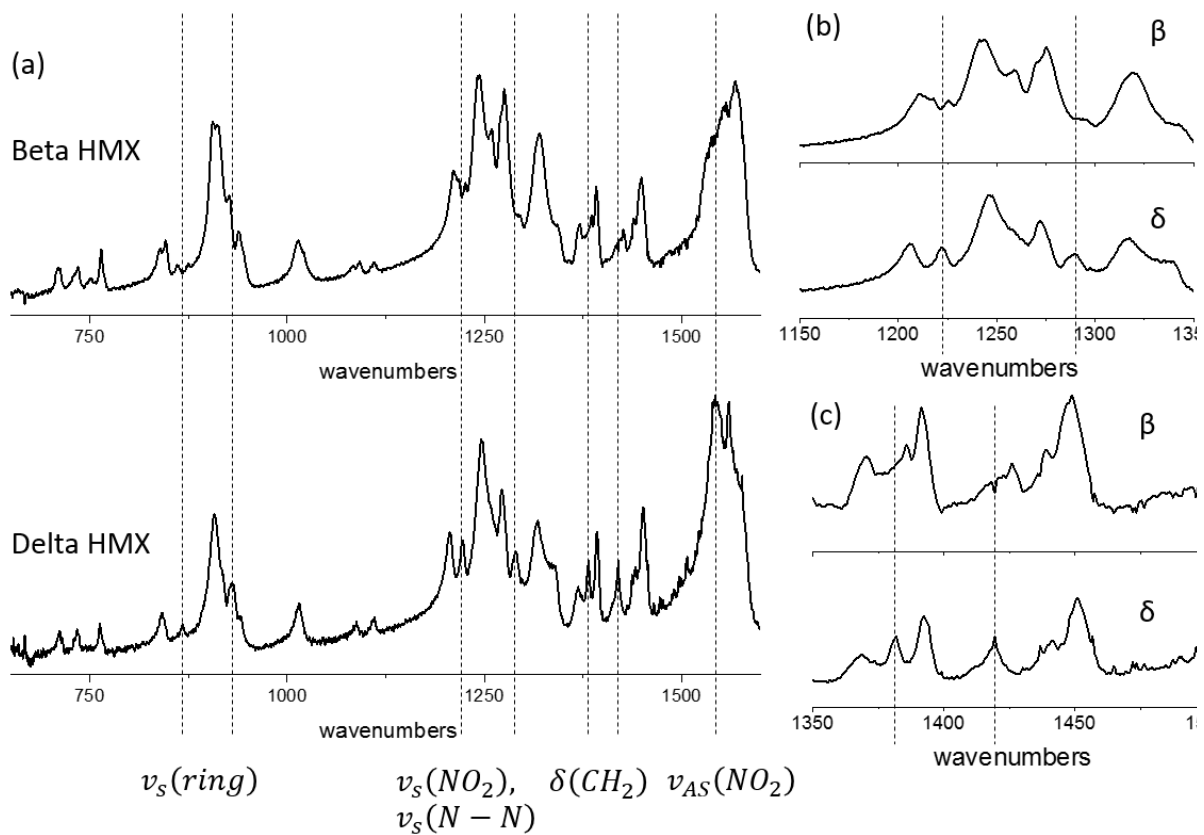**Figure 2.1.** A diagram of the laser setup for 3D spectroscopy experiments
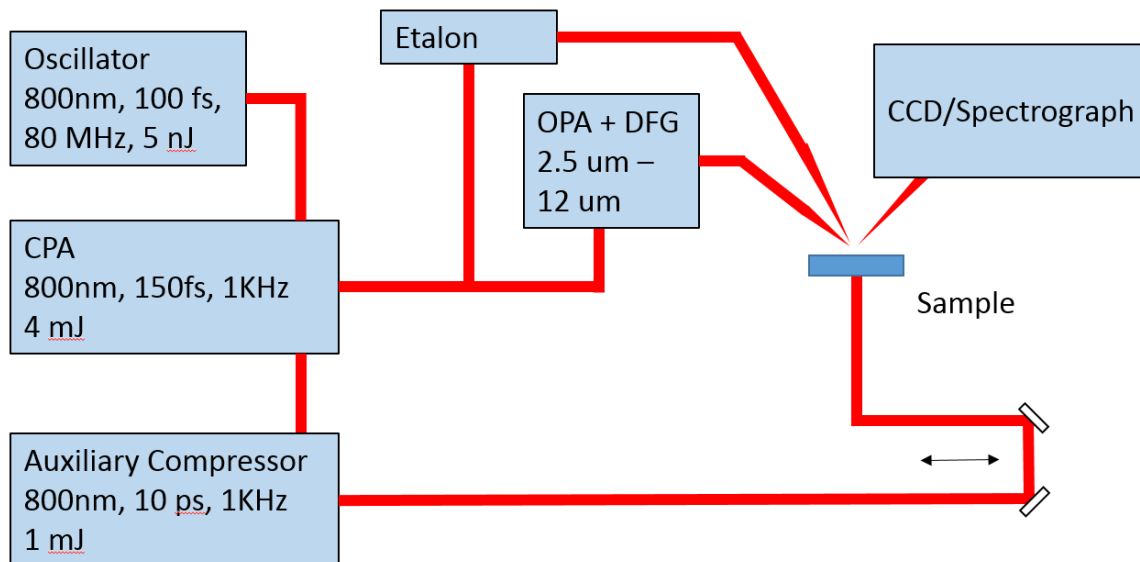
Figure 2.2. A diagram of the laser setup for laser driven shock experiments

Figure 2.3. A diagram of the sample design for laser driven shocks

Figure 2.4. A diagram of the system and sample design for flyer plate driven shocks

Figure 2.5. (a) IR spectrum of sprayed layers of δ-HMX and β-HMX with dashed lines indicating significant peak shifts, with emphasis on (b) the nitro stretch region and (c) the methyl bend region

Chapter 3: IR-Raman Pump Probe Spectroscopy

3.1 Introduction:

IR-Raman spectroscopy is a technique where an initial IR pulse pumps a specific vibration or set of vibrations, and time delayed visible pulses, via Raman scattering, probe all Raman active vibrational modes to determine time dependent occupation. By changing the set of vibrations initially pumped and observing the time dependent evolution of excited states, a picture of energy flows within the molecule can be created.

The dynamics of vibrational energy flow are extremely important for a variety of research topics such from reaction rate theories[2] to molecular electronics[3-5]. To design molecular scale devices such as thermal diodes[6] or molecular wires[3-5], vibrational energy flow must be understood to the level where it can be predicted and controlled. If building blocks for such devices could be created such that they could be combined and the result behaved in a predictable way, such devices could be far more easily modified and improved.

Towards this end, substituted benzenes make for an excellent model system. Energy flows in benzene itself has been extensively studied by the Dlott group[7,8] and others[9-11], and thus the effects of substitutions and other structural perturbations on the benzene ring can be explored.[12-15] Phenyl rings are also often incorporated into molecular scale devices such as molecular wires, where efficient energy flow is vital and poor energy dissipation can easily damage or decrease the functionality of a wire.[3,16] Understanding substituted benzenes is also of significant benefit in

the realm of energetic materials, with systems such as trinitrotoluene (TNT) or dinitroanisole (DNAN) that are composed of a phenyl ring with attached nitro groups. How the energy flows in these molecules is key to understanding their behavior, especially during initiation where nonequilibrium energy distributions in certain functional groups can occur.[17,18]

3.2 Prior Work:

IR-Raman spectroscopy has been used for many decades to observe energy flows. From 1974-1978 Laubereau and coworkers[19,20] developed a way to generate intense picosecond IR laser pulses that could excite CH- and OH-stretches in molecules. They were able to use this to observe time dependent vibrational relaxation processes in ethanol and chloroform, representing the first IR-Raman experiments. Since then significant improvements have been made using amplified Ti:Sapphire lasers to generate tunable IR and visible pulses allowing for much finer control, proving especially valuable for techniques used in this work such as 3D IR-Raman, which requires a wide ranges of accessible IR frequencies to pump many different parent states.[12,13,15,21]

One potential issue with this technique is potential bias in observed states, as only Raman active modes can be observed. While asymmetric functional groups such as nitro allow us to observe all relevant modes, something like a phenyl ring has an inversion center, and thus a significant number of Raman inactive modes. The group has previously used ultrafast calorimetry to demonstrate that the observed energy in Raman active modes is representative of all energy flows within the molecule for benzene. By using a molecular thermometer, CCl4,[8,22-24] it was

possible to monitor the total energy lost from IR-pumped benzene over time,[7] and establish that the time dependence of the energy in non-Raman active modes was the same as the observable energy.

The Dlott group has in the past demonstrated this technique on a series of aryl halides X-Ph (X = F, Cl, Br, I), and was able to observe ring and functional group vibrations following excitation of the symmetric ring CH stretching mode. This was followed up by a series of experiments that demonstrate energy transfer throughout the molecule can be highly dependent on the initial parent state. [12,13,15,21]

3.3 Theoretical Basis:

Raman spectroscopy observes transitions to higher (Stokes) and lower (Anti-Stokes) vibrational states after scattering events. While Stokes transitions can be observed from any intitial state, Anti-Stokes transitions cannot be observed from the ground state. For organic liquids, the majority of vibrational modes have energy levels well above KT at room temperature, and as such are mostly in the ground state. Thus when a vibrational mode is excited either directly or indirectly from a parent mode, a significant rise in Anti-Stokes signal can be seen. While a change can also be observed from the Stokes spectrum, the large ground state population means that it is a proportionally much smaller change. Thus when accounting for minor fluctuations in signal, the Anti-Stokes spectrum is a far more sensitive measure of excited state populations and is able to quantitatively measure excited state populations.

For any given probe pulse with frequency ω_L, at a time t relative to the arrival of the pump pulse, the intensity of the Stokes and Anti-Stokes signals are respectively

$$I_\omega^S(t) \propto \omega_L(\omega_L - \omega)^3[n_\omega(t) + 1]\sigma_R$$

$$I_\omega^{AS}(t) \propto \omega_L(\omega_L + \omega)^3 n_\omega(t)\sigma_R$$

where σ_R is the Raman scattering cross section at ω_L and $n_\omega(t)$ is the occupation number of a vibration with frequency ω in the excited state. The constant of proportionality depends on the experimental system and is equal for both. At room temperature, $n_\omega(t_0) \ll 1$ for almost all vibrational modes studied, and thus we can say

$$n_\omega(t) = \frac{I_\omega^{AS}}{I_\omega^S}\left[\frac{(\omega_L - \omega)}{(\omega_L + \omega)}\right]^3$$

That is, the ratio of the Anti-Stokes intensity to the Stokes intensity at is proportional to the occupation number for that vibrational mode. Thus we are essentially able to quantitatively probe occupation number for any vibrational mode over time.

To actually interpret energy flow using time resolved occupation numbers, the Dlott group developed a three-stage model[25-27] shown in Figure 3.1. Vibrational states are assigned one of four types based on previous work.[28] The first is the high energy states, composed of parents states excited by the pump pulses, with energies in the 2000-4000 cm^{-1} range. The second and third are the mid and lower energy states at 1000-1600 cm^{-1} and < 1000 cm^{-1} respectively. Fourth is the continuum of low energy states that make up the bath.

In three stage model, we start with the parent high energy states being exited by the pump pulses. Once the parents are excited, the population begins to fall with lifetime τ_{IVR} as it

excites other strongly coupled vibrational modes via intramolecular vibrational relaxation (IVR), consisting of mid and lower energy states with essentially no bath states included. This occurs on the timescale of 1-3 ps in the substituted benzenes studied. [12,13,15,21]

In the second stage, the populations of the mid energy daughter states fall with lifetime on order 5-10ps for these substituted benzenes, exciting second generation low energy daughter states and bath states, while the populations first generation low energy daughter states fall, exciting bath states. Finally during the third stage, the remaining populations of low energy daughter states decay and excite bath states, occurring on the 20-50 ps time scale for substituted benzenes. Both the second and third stages occur via both intra and intermolecular processes, which can not necessarily be distinguished via IR-Raman experiments.

All of the parameters of this model could be coupled and fit, and this was performed with a few simplifying assumptions in previous works. However, it is fairly sufficient to fit the growth and decay of vibrational mode populations, comparing their lifetimes to determine how the energy is moving, as well as determining approximate quantum yields by comparing relative occupation numbers.

As these molecules are in liquid, there will be intermolecular energy transfer. This results in some energy transfer not accounted for by this model, primarily in the form of an increase in temperature across the entire system. For this reason our studies are primarily confined to the first several picoseconds, where the intramolecular energy flows from excited modes dominate. These intermolecular effects would not be present for the majority of actual use cases, such as molecular wires, but we still must account for them in our experiments.

3.4 3D IR-Raman Spectroscopy:

In prior works, the molecule was probed using a small number of pump wavelengths that specifically targeted functional groups on the molecule. It was asserted that regardless of the pump wavelength used to excite a specific functional group, rapid energy exchange would cause similar results downstream.[19,20,29,30] However, this was demonstrated to be inaccurate when IR-Raman experiments pumped two different CH-stretches in methanol and observed significantly different results.[31] While it was shown in an aryl-halide study that small shifts in pump wavelength did not change downstream effects,[14] this cannot be assumed to be generally true for substituents on molecules, especially in more complex spectra regions

To measure the effects of the pump wavelength in the IR-Raman experiments, it would be optimal to have a full IR-Raman spectrum collected at a continuous range of pump wavelengths. By taking these with a range of delays, everything can be combined into 3D IR-Raman spectra, where the three dimensions are pump wavelength, probe wavelength, and time. These spectra could be used to easily visualize the vibrational relaxation pathways for molecules, providing insight into energy flow throughout the molecule.

Here, 3D IR-Raman spectroscopy is applied to nitromethane (NM) and acetonitrile (MeCN), as well as their fully deuterated analogs d_3-NM and d_3-MeCN in order to demonstrate the technique. These compounds have been previously studied in the Dlott group,[8,22,23,25,32,33] where vibrational relaxation pathways of each liquid were probed using two different pump wavelengths. The details of the intramolecular energy flows will not be discussed here, though this is available from the plots. Instead, the focus will be on the nature of 3D IR-Raman

spectroscopy, and how the spectra can be used to understand the energetic pathways in the molecules.

In the liquids studied here, the target range for parent excitations is the fairly crowded area where fundamental methyl stretching modes are overlaid with combinations and harmonics of lower energy modes. Excitations of combination modes is fortunately clearly visible at short times as excitations of the underlying fundamental transitions. For example, in NM and many other nitro group containing molecules, the combination symmetric and asymmetric nitro stretch $(v_S(NO) + v_{AS}(NO))$ near 2950 cm^{-1} would appear at very short delay times (t ≈ 0 ps) as excitations of both the 1560 cm^{-1} $v_S(NO)$ and the 1400 cm^{-1} $v_{AS}(NO)$.[25]

Even though these combination bands have much smaller IR cross sections compared to the methyl stretches, the experimental setup essentially normalizes IR absorption as a consequence of the relative penetration depths of the pump and the probe.[22] The Raman probe pulses are nonresonant and probe the entire thickness of the sample, while the IR penetration depth for the pump pulses is far shorter and causes the entire IR intensity to be absorbed even for weaker absorptions.[22] So long as the IR penetration depth at a wavelength is shorter than the sample thickness (50 um), the same number of excited molecules will be generated and probed. This allows investigation of otherwise difficult to access combination modes, and could in theory be extended to even thicker samples for even weaker modes.

Depending on the liquid, the absorption of this IR pulse leads to a bulk temperature jump, typically ΔT = 10-40K for the IR-Raman experiments. The size of the temperature jump generally depends on the IR absorption at that wavelength. However, as mentioned above, the thickness

of the sample is significantly longer than the penetration depth even for weak absorptions, and as such most pump wavelengths give the same size temperature jump. The liquids are primarily thermalized after ~10 ps, and so data acquisition was stopped after 10ps. However, previous studies from the Dlott group have shown that small amounts of energy may be trapped in longer-lived excitations, and it's possible that MeCN or NM may not be fully thermalized until 100-200 ps.[8,34] The temperature jump decays by thermal conduction on the 0.1 ms time scale and the interval between pump pulses was 1 ms,[22] so no temperature effects are visible from shot to shot.

The 3D spectra for NM and MeCN, as well as d_3-NM and d_3-MeCN are shown in Figure 3.6-3.9. As the intensities varied over a wide range, the scale is logarithmic. A Stokes Raman spectrum for the molecule runs across the top of each 3D spectrum to show the Raman cross-section for that wavelength. As it is the anti-Stokes spectrums that are plotted, it is important to take the Raman cross-section for vibrational modes into account in order to interpret intensities. The IR absorption spectrum runs along the left side of the last 3D spectrum and provides a reference for the ΔT dependence on IR absorption as mentioned above. The pump wavelength diagonal runs along the right side of each time slice and unlike 2D IR spectra,[35] only the $\nu = 1 ->$ 0 (anti-Stokes) transitions are shown, as opposed to both $\nu = 1 -> 0$ and $\nu = 0 -> 1$ on opposite sides of the pump diagonal.

3.5 Artifacts in 3D Spectroscopy:

There are several types of artifacts visible in the 3D spectra that must be accounted for to avoid confusion. These artifacts are created by processes that can be broadly described as nonlinear light scattering (NLS).[36] NLS is defined as scattered light at frequencies other than those present in the incident laser pulses. Some nonlinear laser processes produce coherent beams. We have carefully arranged the geometry of our apparatus to minimize the detection of such coherent beams, but in a liquid medium, the scattered light from a coherent signal can be detected and can compete with the anti-Stokes signals.

SFG, four-wave mixing (4WM) and self-phase modulation (SPM), were all observed at one time or another in Figures 3.6-3.9. Artifacts are referred to here to mean intensity in the anti-Stokes region that does not originate from vibrational populations. These artifacts can be clearly identified as they decay with optical dephasing time constants T_2 rather than vibration population time constants T_1. They are generated by nonlinear optimal processes, and the intensity of the pump and probe pulses are high enough that even higher order processes are visible.

SFG comes from the second-order nonlinear susceptibility χ^2. In SFG literature, where liquid surfaces and interfaces are studied, it is frequently mentioned that χ^2 vanishes in nonchiral liquids, but that is only true in the dipole approximation.[37] Quadrupole and other higher-order terms in the polarization expansion can lead to weak SFG. SFG generates signals at $\omega_{IR} + \omega_{VIS}$, which corresponds to anti-Stokes wavenumber ω_{IR}. This is the same wavenumber as the parent vibrational excitations generated by IR pump pulses, but only appear near t=0 (when IR and

visible pulses are temporally overlapped), and thus the populations of the excited parent state can be determined from later times.

A 4WM artifact depends on χ^3, which is nonvanishing in all liquids, so the 4WM artifacts in liquids can be more intense than SFG artifacts. A signal at $2\omega_{IR} + \omega_{VIS}$ would appear at the anti-Stokes wavenumber $2\omega_{IR}$, which is generally outside of the detected range for the tunable range of the pump pulses, and should in principle be rejected by the spectrograph used in these experiments. However because the spectrograph is imperfect, 4WM artifacts can sometimes be observed in anti-Stokes spectra as long decaying tails extending into spectrum from the higher wavenumber region. The 4WM artifacts are also observed only near t = 0.

The SPM artifacts are related to the ubiquitous issue of Rayleigh scattering backgrounds in Raman spectroscopy. These backgrounds are signals in a Raman spectrum that tail off from a maximum at zero wavenumbers. In our Raman system, as in most others, a notch filter was used to suppress Rayleigh scattering. However when the probe pulses were intense, SPM caused the probe spectrum to broaden, and sometimes this broadened light was transmitted through the notch filter. SPM artifacts look like Rayleigh scattering backgrounds, and are time-independent. The SPM effect can eliminated by attenuating the probe pulses, but due to the weak signals in our experiments, we run the probe intensity right up to the SPM threshold, and occasionally a laser or sample jet fluctuation will create an SPM artifact. Near t = 0, when the pump and probe pulses are time-coincident, the electric fields of the pump pulses enhance SPM of the probe pulses. This type of pump-enhanced SPM artifact also appears as a Rayleigh scattering background, but the pump-enhanced SPM artifact has an intensity maximum at t = 0.

3.6 3D Spectroscopy Discussion:

A. IR and Raman Spectra

In order to understand and discuss IR-Raman data, it is essential to have at hand plots of the conventional IR and Raman spectra for each sample accompanied by vibrational assignments. Figures 3.2-3.5 show these spectra for NM and MeCN. Figures 3.2-3.4 are adapted from prior publications[23,25], and Figure 3.5 is new. The IR spectra were obtained using FTIR with 4 cm^{-1} resolution, so the observed linewidths were equal to the natural linewidths. The Raman spectra were obtained using picosecond pulses. As a result of the picosecond pulse bandwidth, the Raman resolution was degraded[23] to ~20 cm^{-1} and frequently this broadened the observed transitions. The spectral assignments for NM and d$_3$-NM[38-43], and MeCN and d$_3$-MeCN[44,45] were taken from prior literature studies.

A few aspects of these spectra are worth mentioning. In the CH-stretch region (~2900 cm^{-1}) and the CD-stretch region (~2200 cm^{-1}), the NM spectra are more congested than the MeCN spectra. For example, compare some of the sharper MeCN IR absorption bands near 3000 cm^{-1} in Figs. 4a and near 2200 cm^{-1} in Fig. 5a to the corresponding broader NM bands in Figs. 2a and 3a. In those regions spectral assignments are not simple, and even today not entirely conclusive. Nearby or directly underneath the CH-stretch and CD-stretch fundamentals are numerous overtones and combinations of the lower-energy modes. Ordinarily the IR absorption coefficients for these overtones and combinations would be small, but they can borrow intensity from the fundamental transitions. So pumping in this region with IR pulses does not create simple CH-stretch or CD-stretch excitations, but rather an admixture of them with lower-energy

states. The most well-known example of this effect arises from the 2:1 Fermi resonance between CH-stretch and CH-bend (or CD-stretch and CD-bend), where, as observed in both NM[8,25] and MeCN[23,33], pumping the stretch transition promptly creates bend excitations as well. Another important factor is that in NM, the nitro-stretches near 1500 cm^{-1} are so close in energy to the CH-bends that they are strongly mixed, and a CH-stretch/nitro-stretch 1:2 resonance is also possible.

With d_3-NM (Fig. 3) the CD-bend CD-bends are downshifted enough to become well-separated from the nitro-stretches, and also from the CN-stretch. However there is another kind of mixing. The CD-bends near 1100 cm^{-1} are resonant with the methyl rocking $\rho(CD_3)$, which was 1104 cm^{-1} in NM.

In MeCN (Fig. 4) there is a 2:1 Fermi resonance between $\nu_a(CH_3)$ and $2\delta_a(CH_3)$, but not between $\nu_s(CH_3)$ and $2\delta_s(CH_3)$.[23] As a result, the $\nu_a(CH_3)$ and $\delta_a(CH_3)$ transitions are noticeably broader than $\nu_s(CH_3)$ and $2\delta_s(CH_3)$. The same pattern is seen in d_3-MeCN (Fig. 5). In MeCN the CN-stretch is an isolated excitation, but in d_3-MeCN the CN-stretch is close to and strongly mixed with the CD-stretch $\nu_a(CD)$.

B. Nitromethane

We will first consider the shorter-time (0,1 ps) NM spectra in Fig. 6 as the IR pump pulses were scanned through the CH-stretch region, from 3200 cm^{-1} to 2700 cm^{-1}. At 3200 cm^{-1}, well above the nominal CH-stretch absorption, there are no clearly-evident absorption bands (Fig. 2a), but nonetheless Fig. 6 shows excitations promptly appearing in $\nu(CN)$, $\delta(NO_2)$ and $\rho(NO_2)$. Thus there must be a combination-band transition near 3200 cm^{-1} that combines the character of

these three modes. This example illustrates the ability of shorter-time 3D IR-Raman spectroscopy to detect and characterize weak combination-band transitions. At 3100 cm^{-1} there is a diagonal signal, but very little population in the lower-wavenumber modes, so the diagonal signal at 3100 cm^{-1} was primarily an SFG artifact. At 3000 cm^{-1}, where the IR pulses were near the absorption maximum of $\nu_a(CH_3)$, the 3D spectrum shows that both $\nu_a(CH_3)$ and $\nu_s(CH_3)$ were excited. This is a consequence of spectral overlap between the $\nu_a(CH)$ absorption peak and the higher-energy tail of $\nu_s(CH_3)$. This 3000 cm^{-1} excitation condition also promptly produced all lower-wavenumber vibrations except 607 cm^{-1} $\rho(NO_2)$. At 2900 cm^{-1}, pumping into the absorption maximum of $\nu_s(CH_3)$, we saw little $\nu_a(CH_3)$ but we did see all lower-wavenumber vibrations except $\rho(NO_2)$, with 1402 cm^{-1} (symmetric CH-bend/nitro-stretch) especially prominent. At 2800 cm^{-1} we promptly saw all lower-wavenumber vibrations except 1562 cm^{-1} (asymmetric CH-bend/nitro-stretch) and 607 cm^{-1} (nitro-bend). At 2700 cm^{-1}, something interesting happened. A great deal of excitation appeared at 1402 cm^{-1}, even though there was little CH-stretch excitation, which suggests that we pumped and observed the first overtone of the 1402 cm^{-1} CH-bend/nitro-stretch transition.

Looking at the longer-time spectra in Fig. 6, we saw NM proceeding toward a thermalized state. It is interesting that $\rho(CH_3)$ at 1104 cm^{-1} was never excited at shorter times, indicating that this excitation is practically decoupled from the other normal modes. It is possible that the later-time excitation of $\rho(CH_3)$, as the NM approaches thermalization, results solely from phonon up-pumping of lower-energy excitations.

Looking at the intensity profiles along the vertical stripes of the lower-wavenumber bands, recall these spectra are plotted using a logarithmic intensity scale, which flattens out the

pump wavenumber dependence of the intensity. Once the NM has thermalized one would expect these intensity profiles to approximately track the IR absorption spectrum in Fig. 2a, which has a maximum at 2968 cm^{-1}, a much weaker maximum at 3050 cm^{-1}, and little intensity above 3150 cm^{-1} or below 2850 cm^{-1}. In fact this is not quite what is observed. All the lower-wavenumber signals at longer delay times (except $\rho(CH_3)$ do have maxima near at 2968 cm^{-1} and 3050 cm^{-1}, but they also have excess populations below (e.g. 2750 cm^{-1}) and above (e.g. 3200 cm^{-1}) the CH-stretch resonances. Populating the lower-wavenumber excitations by pumping in this region surely indicates that combination bands are being excited, and the magnitude of the lower-wavenumber population results from the enhanced sensitivity of IR-Raman spectroscopy to weaker IR absorption transitions.

C. d$_3$-Nitromethane

With d$_3$-NM (Fig. 7), we will first consider the shorter-time spectra at t = 0,1 ps, as the IR pulses were tuned from 3000-2150 cm^{-1}. As shown in Fig. 3b (and at the top of Fig. 7), between 3000 cm^{-1} and 2400 cm^{-1} the only transitions in this deuterated solvent were overtones and combinations of nitro stretches. By tuning through this range, the 3D spectrum confirmed the assignments we proposed in Fig. 3b. When the band near 3000 cm^{-1} that we proposed to be $2\nu_a(NO_2)$ was excited, only $\nu_a(NO_2)$ was observed. Similarly at 2900 cm^{-1}, proposed to be $\nu_a(NO_2)$ + $\nu_s(NO_2)$, both $\nu_a(NO_2)$ and $\nu_s(NO_2)$ were observed. At 2700 cm^{-1}, proposed to be $2\nu_s(NO_2)$, only $\nu_s(NO_2)$ was observed.

At IR pump wavenumbers where CD-stretches were excited, the dominant daughter excitations generated by VET were the ~1400 cm^{-1} nitro-stretches, and there was hardly any excitation of the ~1100 cm^{-1} CD-bends.

Comparing Figs. 6 and 7 results in a quite interesting observation about CH-stretch relaxation of NM compared to CD-stretch relaxation of d$_3$-NM. The usual expectation would be that CH-stretch pumping would primarily generate CH-bend excitations, and CD-stretch pumping would primarily generate CD-bend excitations.[20] But in NM the nitro-stretch excitations are resonant with the CH-bend states, whereas in d$_3$-NM the nitro-stretch excitations are in the region between CD-stretches and CD-bends. So the question can be posed, is the relaxation of a CH-stretch or CD-stretch excitation on the methyl group more likely to involve the methyl group itself or the adjacent nitro group? With NM it is impossible to tell because there is so much coupling between the nitro-stretch and methyl-bend, but with d$_3$-NM it is clear that CD-stretch relaxation to the adjacent nitro group is much more efficient than to bends on the same methyl group.

D. MeCN

MeCN (Fig. 8) was scanned from 3600-2150 cm^{-1}. The vertical stripes in the MeCN spectra were more patchy than with NM (Fig. 6). This is a reflection that the MeCN IR absorption spectrum in the pumped region (Fig. 4a) is less congested than NM (Fig. 2a). In the first 0,1 ps, with 3600 cm^{-1} pumping, well above CH-stretch absorbances, a diagonal signal was seen but it was not entirely SFG artifact, since the corresponding horizontal stripe shows some excited-state populations of ν(CN) and δ(CCN). Since ν(CN) is 2253 cm^{-1}, the most likely origin would be a

combination with $\delta_s(CH_3)$ (1312 cm^{-1}), but the shorter-time 3D spectrum in Fig. 8 with 3600 cm^{-1} pumping showed very little excitation near 1312 cm^{-1} and quite a bit at 379 cm^{-1}. Thus this excitation seemingly involved $\nu(CN)$ with at least one and probably multiple quanta (up to 3) of 379 cm^{-1} $\delta(CCN)$ bending excitations. Moving the pump wavenumber lower, nothing much was seen until the CH-stretches came into resonance. The higher-energy CH-stretches produced mainly $\nu(CN)$ and $\nu(CC)$, whereas the lower-energy CH-stretches produced mainly CH-bends. Pumping the region just below the CH-stretches (2800-2400 cm^{-1}) produced little vibrational excitation except near 2600 cm^{-1} where a small amount of $\nu(CN)$ and $\delta(CCN)$ appeared, indicating that 2600 cm^{-1} IR pulses pumped the $\nu(CN) + \delta(CCN)$ combination. Nothing much was seen below 2400 cm^{-1} until the 2253 cm^{-1} $\nu(CN)$ transition was pumped, and at that point we promptly observed $\delta_s(CH_3)$ and $\nu(CC)$. Looking at the longer-time data, the primary daughter excitations from CH-stretch pumping and from CN-stretch pumping were CH-bends and $\nu(CC)$.

E. d$_3$-MeCN

The d$_3$-MeCN spectrum in Fig. 9 was scanned from 3400-2000 cm^{-1}. At the highest wavenumbers 3400-2600 cm^{-1}, the 3D spectra confirm the assignments given in Fig. 5b and at the top of Fig. 9, where we have indicated combination bands of $\nu(CN)$ with $\delta(CCN)$, $\nu_s(CC)$ and $\delta_s(CD)$. When we pump the CD-stretch and CN-stretch regions, the other prompt excitations were small amounts of CD-bend, CC-stretch and CCN-bend. Looking at the longer-time data we see than when the CD-stretch and CN-stretch excitations decayed they produced CD-bends, CC-stretches and CCN-bends.

3.7 Conclusions:

3D spectroscopy is an exceptional tool for tracing and visualizing energy flows through a molecule. Even when the initial excitation was a combination band or overtone, and even when those bands were very weak in the IR absorption spectrum, the 3D spectra did a remarkable job of characterizing which excitations were produced when those weak bands were pumped. The spectra provide information about vibrational relaxation pathways at a glance, and make it easy to characterize which parent excitations lead to which daughter modes.

3.8 References:

(1)   Sun, Y.; Pein, B. C.; Dlott, D. D. *The Journal of Physical Chemistry B* **2013**, *117*, 15444.
(2)   Voth, G. A.; Hochstrasser, R. M. *The Journal of Physical Chemistry* **1996**, *100*, 13034.
(3)   Segal, D.; Nitzan, A. *The Journal of Chemical Physics* **2002**, *117*, 3915.
(4)   Segal, D.; Nitzan, A.; Hänggi, P. *The Journal of Chemical Physics* **2003**, *119*, 6840.
(5)   Michael, G.; Mark, A. R.; Abraham, N. *Journal of Physics: Condensed Matter* **2007**, *19*, 103201.
(6)   Segal, D.; Nitzan, A. *The Journal of Chemical Physics* **2005**, *122*, 194704.
(7)   Seong, N.-H.; Fang, Y.; Dlott, D. D. *The Journal of Physical Chemistry A* **2009**, *113*, 1445.
(8)   Deàk, J. C.; Iwaki, L. K.; Dlott, D. D. *J. Phys. Chem. A* **1999**, *103*, 971.
(9)   Riedle, E.; Neusser, H. J.; Schlag, E. W.; Lin, S. H. *The Journal of Physical Chemistry* **1984**, *88*, 198.
(10)   Sibert, E. L.; Reinhardt, W. P.; Hynes, J. T. *The Journal of Chemical Physics* **1984**, *81*, 1115.
(11)   Callegari, A.; Merker, U.; Engels, P.; Srivastava, H. K.; Lehmann, K. K.; Scoles, G. *The Journal of Chemical Physics* **2000**, *113*, 10583.

(12)   Pein, B. C.; Sun, Y.; Dlott, D. D. *J. Phys. Chem. A* **2013**, *On Line ASAP DOI: 10.1021/jp3127863*.

(13)   Pein, B. C.; Sun, Y.; Dlott, D. D. *The Journal of Physical Chemistry B* **2013**, *117*, 10898.

(14)   Pein, B. C.; Seong, N.-H.; Dlott, D. D. *The Journal of Physical Chemistry A* **2010**, *114*, 10500.

(15)   Pein, B. C.; Dlott, D. D. *The Journal of Physical Chemistry A* **2014**, *118*, 965.

(16)   Ioffe, Z.; Shamai, T.; Ophir, A.; Noy, G.; Yutsis, I.; Kfir, K.; Cheshnovsky, O.; Selzer, Y. *Nat Nano* **2008**, *3*, 727.

(17)   Dlott, D. D. *Multiphon up-Pumping in Energetic Materials*; Thompson, D.; Brill, T.; Shaw, R., Eds. World Scientific: Hackensack, New Jersey, 2005.

(18)   Dlott, D. D. *Fast Molecular Processes in Energetic Materials*; Politzer, P.; Murray, J. S., Eds. Elsevier: New York, 2003.

(19)   Laubereau, A.; Kehl, G.; Kaiser, W. *Opt. Commun.* **1974**, *11*, 74.

(20)   Laubereau, A.; Kaiser, W. *Rev. Mod. Phys.* **1978**, *50*, 607.

(21)   Pein, B. C.; Dlott, D. D. In *Ultrafast Infrared Vibrational Spectroscopy*; Fayer, M. D., Ed.; CRC Press Taylor & Francis Group: Boca Raton, FL, 2013, p 269.

(22)   Deàk, J. C.; Iwaki, L. K.; Rhea, S. T.; Dlott, D. D. *J. Raman Spectrosc.* **2000**, *31*, 263.

(23)   Deàk, J. C.; Iwaki, L. K.; Dlott, D. D. *The Journal of Physical Chemistry A* **1998**, *102*, 8193.

(24)   Graham, P. B.; Matus, K. J.; Stratt, R. M. *The Journal of Chemical Physics* **2004**, *121*, 5348.

(25)   Shigeto, S.; Pang, Y.; Fang, Y.; Dlott, D. D. *J. Phys. Chem. B* **2008**, *112*, 232.

(26)   Shigeto, S.; Dlott, D. D. *Chemical Physics Letters* **2007**, *447*, 134.

(27)   Fang, Y.; Shigeto, S.; Seong, N.-H.; Dlott, D. D. *The Journal of Physical Chemistry A* **2009**, *113*, 75.

(28)   Nitzan, A.; Jortner, J. *Molecular Physics* **1973**, *25*, 713.

(29)   Graener, H.; Laubereau, A. *Chem. Phys. Lett.* **1987**, *133*, 378.

(30)   Seilmeier, A.; Kaiser, W. In *Ultrashort Laser Pulses and Applications*; Kaiser, W., Ed.; Springer Verlag: Berlin, 1988; Vol. 60, p 279.

(31)   Iwaki, L. K.; Dlott, D. D. *Chem. Phys. Lett.* **2000**, *321*, 419.

(32)   Deàk, J. C.; Iwaki, L. K.; Dlott, D. D. *Opt. Lett.* **1997**, *22*, 1796.

(33)   Deàk, J. C.; Iwaki, L. K.; Dlott, D. D. *Chem. Phys. Lett.* **1998**, *293*, 405.

(34)   Deàk, J. C.; Iwaki, L. K.; Dlott, D. D. *J. Phys. Chem.* **1998**, *102*, 8193.

(35)   Hamm, P.; Zanni, M. T. *Concepts and methods of 2D infrared spectroscopy*; Cambridge University Press: Cambridge, 2011.

(36)   Terhune, R. W.; Maker, P. D.; Savage, C. M. *Phys. Rev. Lett.* **1965**, *14*, 681.

(37)   Shen, Y. R. *The Principles of Nonlinear Optics*; Wiley: New York, 1984.

(38)   Wells, A. J.; Wilson, E. B. *J. Chem. Phys.* **1941**, *10*, 314.

(39)   McKean, D. C.; Watt, R. A. *J. Mol. Spectrosc.* **1976**, *61*, 184.

(40)   Hill, J. R.; Moore, D. S.; Schmidt, S. C.; Storm, C. B. *J. Phys. Chem.* **1991**, *95*, 3037.

(41)   Courtecuisse, S.; Cansell, F.; Fabre, D.; Petite, J. P. *J. Chem. Phys.* **1998**, *108*, 7350.

(42)   Shkurinov, A.; Jonusauskas, G.; Rullière, C. *J. Raman Spectrosc.* **1994**, *25*, 359.

(43)   Miller, P. J.; Block, S.; Piermarini, G. J. *J. Phys. Chem.* **1989**, *93*, 462.

(44)   Herzberg, G. *Molecular Spectra and Molecular Structure II. Infrared and Raman Spectra of Polyatomic Molecules*; Van Nostrand Reinhold: New York, 1945.

(45)   Pace, E. L.; Now, L. J. *J. Chem. Phys.* **1968**, *49*, 5317.

3.9 Figures:
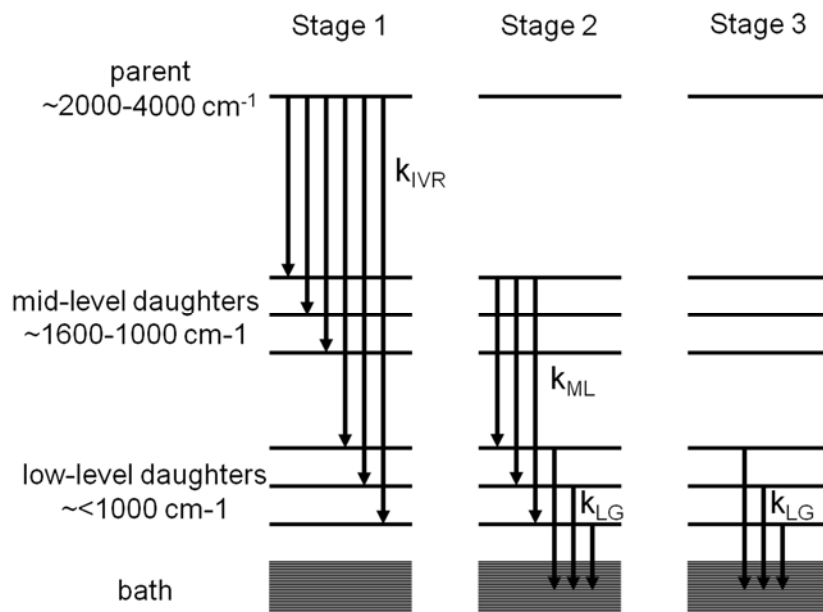
Figure 3.1. Diagram of three-stage model for VR and VC. During stage 1, the pumped parent P decays to the mid- and low-level daughters via IVR processes with a rate kIVR. During stage 2, the now populated mid-level daughters, excited by the parent, excite low-level daughters while the low-level daughters excite the bath with rates kML and kLG respectively. During stage 3, the low-level daughters then continue to excite the bath
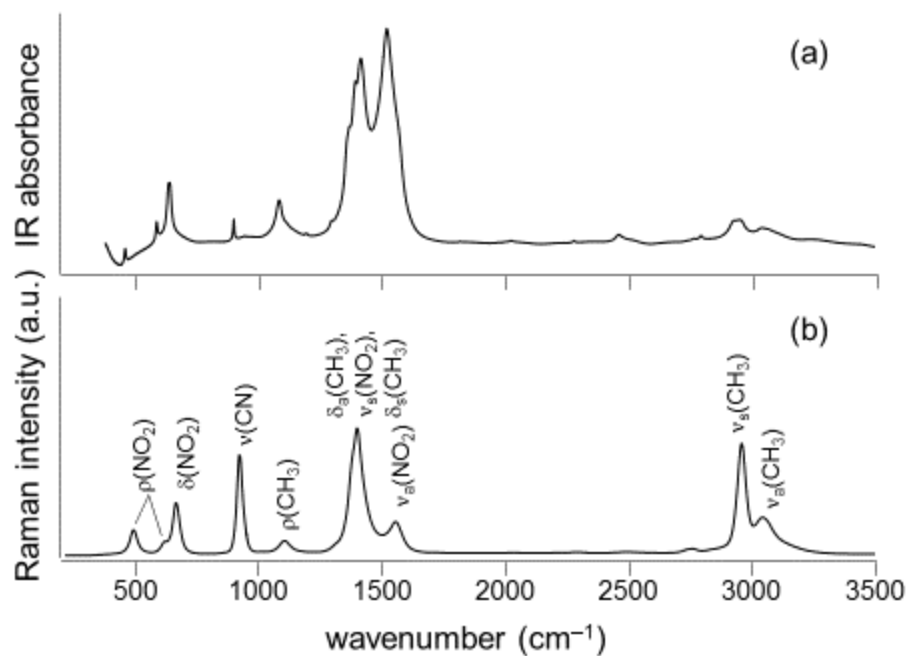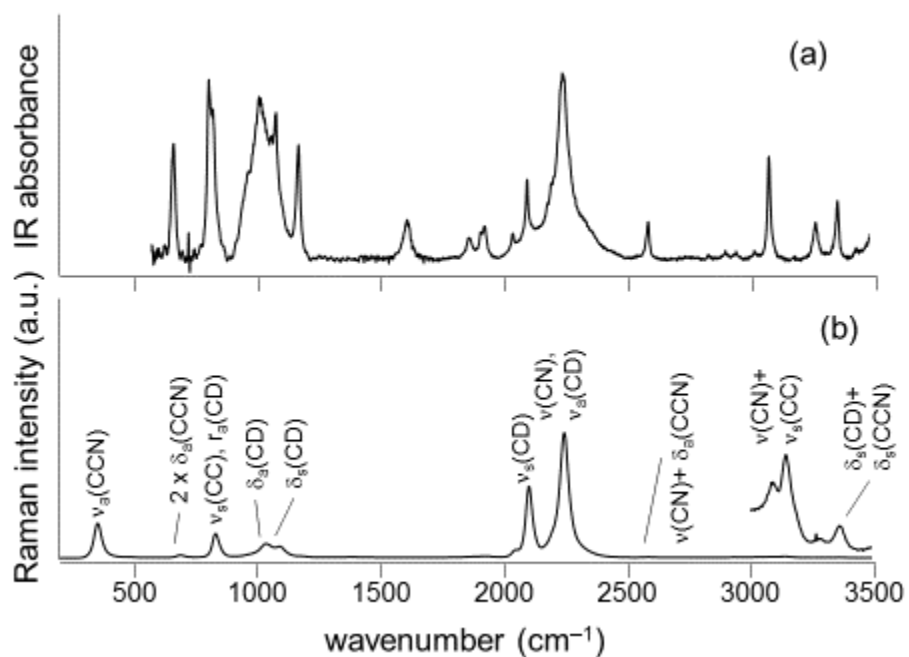
Figure 3.2. (a) Infrared spectrum of nitromethane (NM) with 4 cm^{-1} resolution. (b) Raman spectrum of nitromethane with assignments, obtained using the picosecond laser. The resolution was 20 cm^{-1}
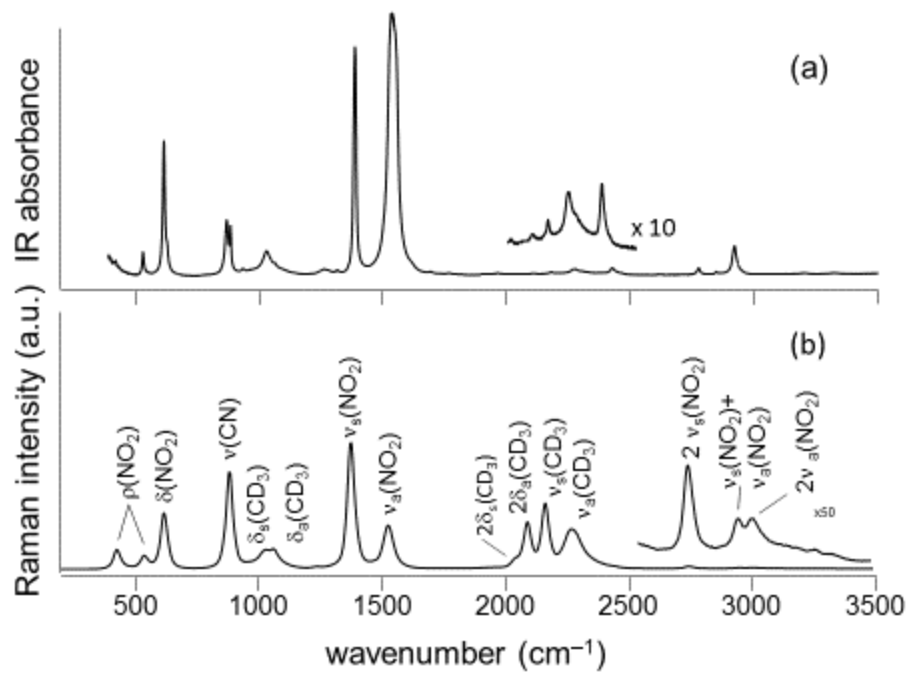
Figure 3.3. (a) Infrared spectrum of d_3-nitromethane (d_3-NM) with 4 cm^{-1} resolution. (b) Raman spectrum with assignments, obtained using the picosecond laser. Nitro-stretch overtones and combination bands could be seen in the ~3000 cm^{-1} region. The resolution was 20 cm^{-1}.
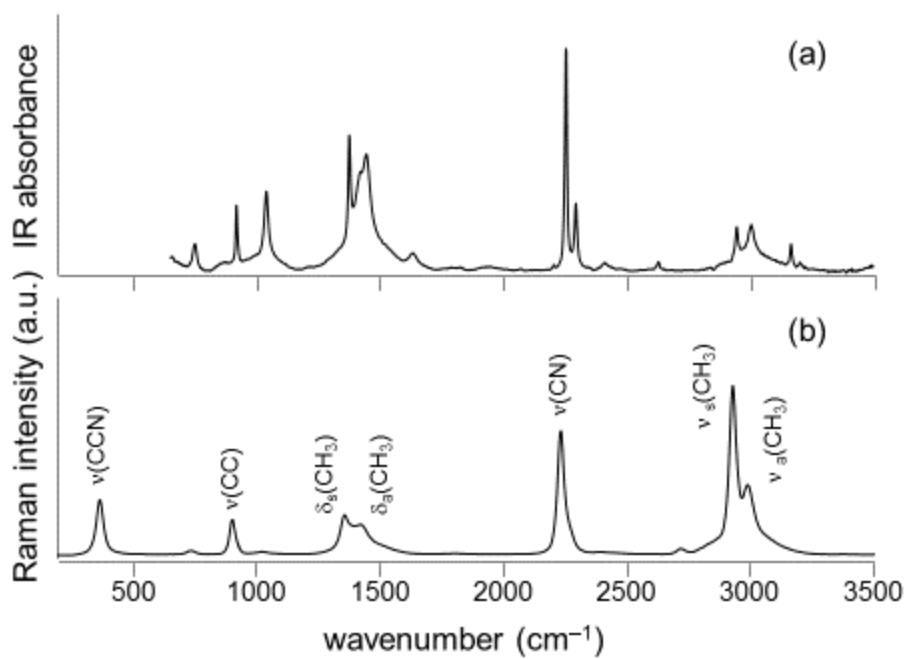
Figure 3.4. (a) Infrared spectrum of acetonitrile (ACN) with 4 cm⁻¹ resolution. (b) Raman spectrum with assignments, obtained using the picosecond laser. The resolution was 20 cm⁻¹.

Figure 3.5. (a) Infrared spectrum of d_3-acetonitrile (d_3-ACN) with 4 cm^{-1} resolution. (b) Raman spectrum with assignments, obtained using the picosecond laser. The resolution was 20 cm^{-1}. Above 2500 cm^{-1}, several overtones and combination bands could be observed, especially those involving v(CN).
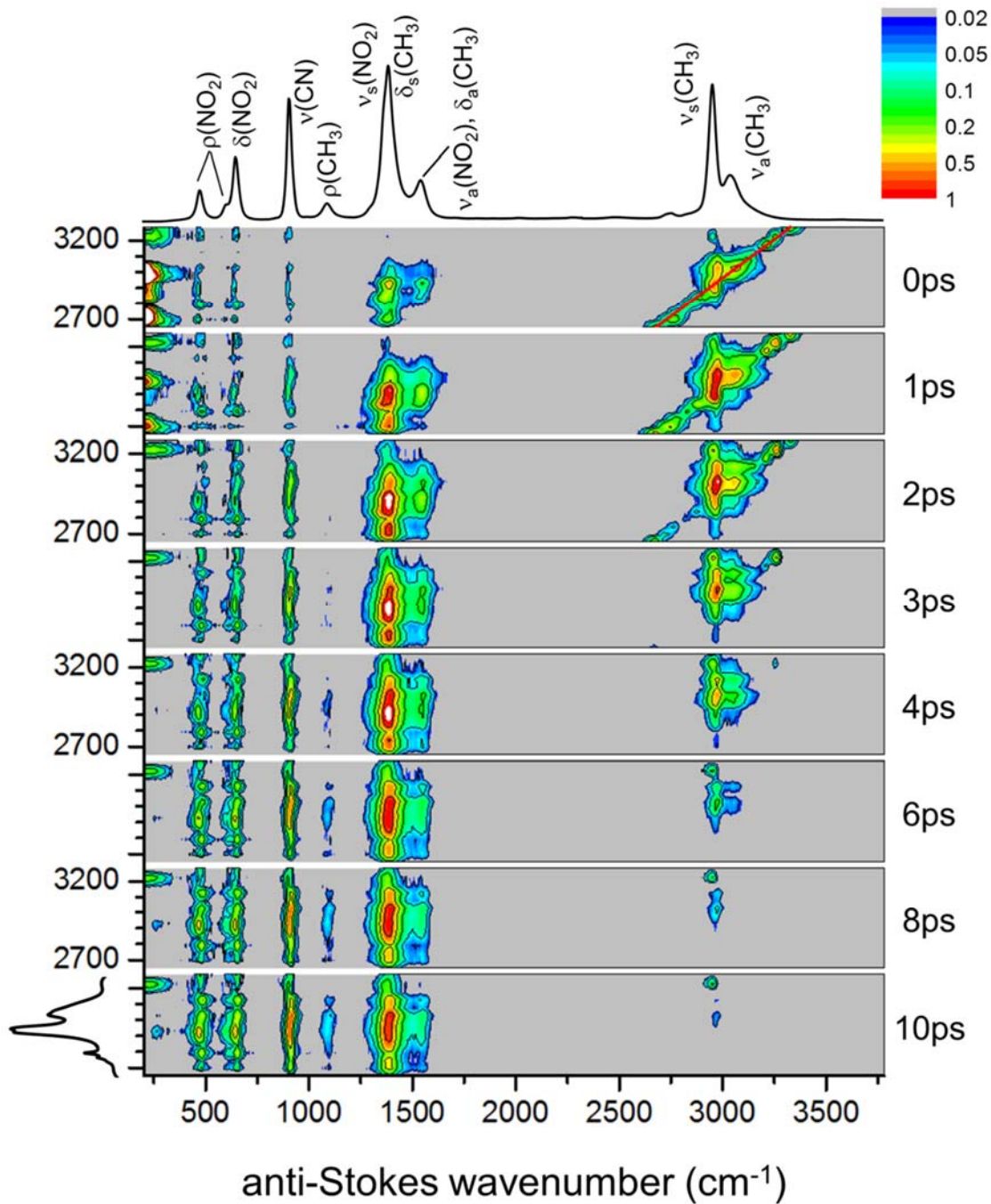
Figure 3.6. 3D IR-Raman spectrum of nitromethane. A reference Raman spectrum with assignments was drawn above the top panel and a reference IR spectrum to the left of the bottom panel. A reference diagonal was indicated in the top panel. Note logarithmic intensity scale.
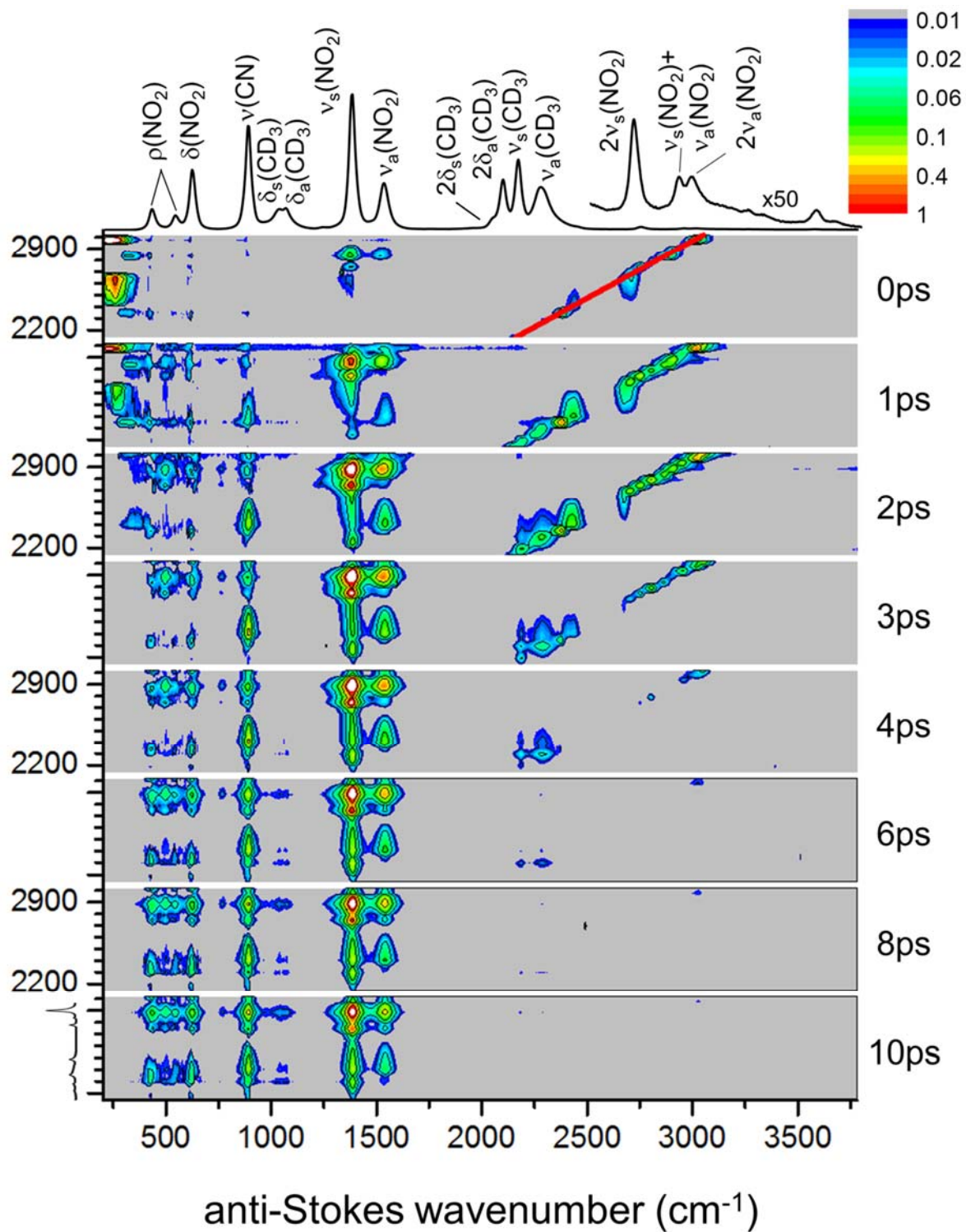
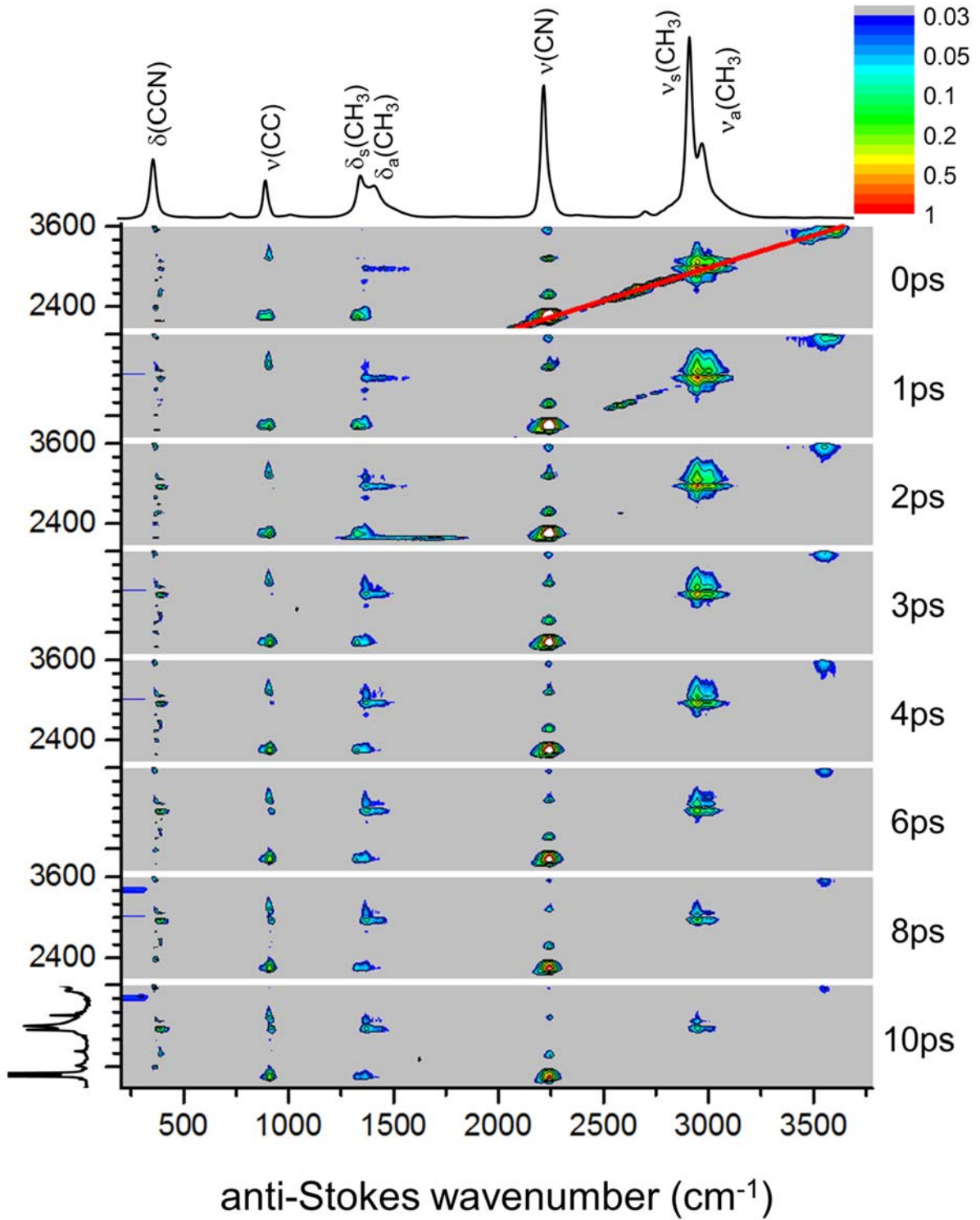**Figure 3.7**. 3D IR-Raman spectrum of d₃-nitromethane.
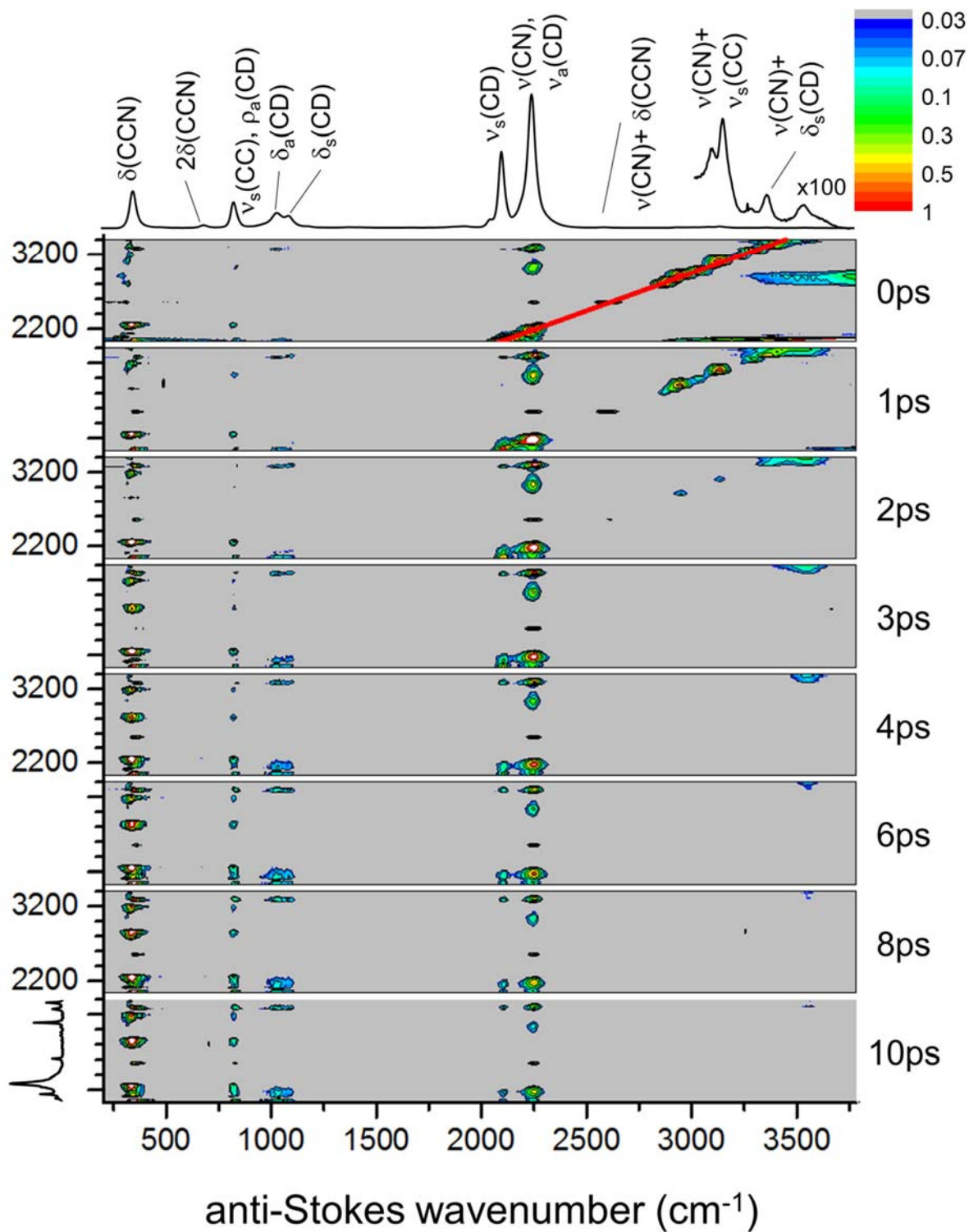
Figure 3.8. 3D IR-Raman spectrum of acetonitrile.

Figure 3.9. 3D IR-Raman spectrum of d₃-acetonitrile.

Chapter 4: Laser Driven Shock Initiation of Molecular Explosives

4.1 Introduction:

Shocks allow for the creation of extreme conditions in both pressure and temperature within materials,[1,2] and can create these conditions to be created on picoseconds time scales. This allows for the investigation of phase transitions[3-5] and chemical reactions[6-8] induced by the extreme conditions. Shock compression experiments have been used to study materials under these extreme conditions as early as 1955.[9]

A common method for generating shock waves on the appropriate time scales is via ultrafast, high energy laser pulses. Large facilities such as the National Ignition Facility at Lawrence Livermore National Laboratory are able to reach laser intensities at the sample of 10^{13}-10^{14} W cm^{-2}, allowing for pressures on the order of terapascals to be produced.[10,11] However, these facilities are expensive to run, difficult to operate, and can fire very few shots per day. If lower pressures are acceptable, table top laser systems have been employed for similar shock compression studies.[12-16] These systems are far cheaper and can fire thousands of shots per minute, but are only able to reach pressures in the 10-100 gigapascal range. The system described here is such a system, able to fire 100 shots per second while creating pressures of a few gigapascals. The ability to average large numbers of shots to improve signal was vital to the research here.

There has been significant work in simulations and modeling of molecular dynamics during the initiation of energetic materials.[17-20] However, there is significant disagreement

between models, and a severe lack of experimental data makes verification and refinement of models difficult. Conventional shock experiments on bulk materials are regularly conducted,[21,22] but have neither the time nor length resolution to aid in mechanistic models of initiation. The primary obstacle for experimental design is that ideally the different layers of molecules behind a shock front should be observable separately, and should be observable on the picosecond time scale to observe the first bond-breaking events.

4.2 Prior Work:

To help develop understanding of the mechanisms of molecular initiation, the Dlott group has been using self-assembled monolayers (SAMs) as models for molecules undergoing shock.[23-25] The monolayers were embedded in an impedance matched sandwich, as seen in Figure 4.1, and have a single distinct functional group that can be tracked spectroscopically. To obtain the requisite time resolution, vibrational SFG was used to track the terminal nitro group of a nitrobenzoic acid monolayer.[26]

The results of the shock compression experiment can be seen in Figure 4.2. The symmetric nitro stretch is being probed, and clearly drops then recovers as the shock shifts the orientation of the molecules. Pressures within the monolayer were calculated both based on Hugoniot measurements,[27] as well as comparisons to data from diamond anvil cell experiments,[28] which gave pressures of 5.6 GPa and 1.7 GPa respectively. With this clear demonstration of the ability of the system to generate shocks within a thin layer and observe them spectroscopically on a picosecond time scale, the next step was to attempt this on an actual energetic material.

4.3 Sample Design and Preparation:

While prior work involving shocked monolayers allowed for fairly simple sample preparation, obtaining thing layers of HMX proved to be significantly more difficult, and the problem was never solved satisfactorily.

The starting point was the sample for shocked monolayers[29], which involved 2" x 2" x 1/16" borosilicate glass squares upon which was deposited 8 nm of chromium and 300 nm of aluminum via e-beam. This was then exposed to a dilute solution of the molecule for several days, after which a thin film of PMMA was applied via spin coating as a shock confinement layer.

The goal of the experiment was to obtain spectra with high time resolution, so the thinnest of HMX layers was desired, with the initial target being 5nm. As previously mentioned, delta HMX was desired. Unfortunately, delta HMX is not the thermodynamically favored state at STP,[30] which unfortunately precludes most methods of forming a thin layer. However previous research indicated that it was possible to obtain delta HMX via rapid evaporation from a spray coater. Furthermore, literature indicated that it might be possible to improve sample coverage by first applying a monolayer to help "pattern" the HMX that was laid down afterwards.[31]

Spray coating was done by hand with an airbrush, which had some issues. First was that the rate of solvent evaporation was heavily dependent on the temperature and humidity of the day, as well as the dryness of the acetone. To somewhat combat this, a heated substrate was used to keep the glass at 35-40° C to speed evaporation and prevent any evaporative cooling of

the glass. The result of this is shown in Figure 4.3. Second, doing the spraying by hand inevitably gave somewhat inhomogeneous and inconsistent results, though this could be controlled for by doing background scans of the sample before running experiments. An example of this inhomogeneity can be seen in Figure 4.4. Lastly, there is a significantly possibility that the actual mix of polymorphs resulting from spray coating depends heavily on the temperature and humidity, which both controls the rate of evaporation as well as the availability of water to form gamma HMX. A robot arm in a climate controlled area would likely be necessary to produce really reproducible spray coated layers.

Initially the approach was to dissolve enough HMX to form a 5nm layer of HMX to form a very dilute solution, in hopes that the additional acetone would allow for a more uniform distribution. However it was discovered that a thin uniform layer was not thermodynamically favored, and additional acetone simply caused aggregation and formation of large HMX islands, as seen in Figure 4.5. Furthermore, monolayers either nitro groups sticking up or carboxylic acid groups sticking up were tested to see if they improved surface coverage. As can be seen in Figures 4.6-4.8, there is no evidence of any improvement. As a result of both of these, the HMX concentration when spraying was increased significantly from 2.77 uM to 3 mM, the total amount of HMX sprayed was increased by a factor of 10, and the monolayer was omitted from future sample preparations.

The polymer layer for the monolayer shock samples was 10% PMMA dissolved in a specialty solvent. This specialty solvent consisted of the following percentages of chemicals by mass: 50% 2-butanone, 15% n-butyl acetate, 15% cyclohexanone and 20% 2-pentanone. This was

unsuitable for coating HMX as HMX was soluble in this specialty solvent, so PVA was substituted as PVA can be deposited from water. There were unfortunately several problems with this.

First was that PVA tended to give polymer layers that were extremely thin. A 20% PVA in water solution only gave polymer layers somewhat less than one micron thick, far from the several microns desired, and even that solution was almost unusably viscous. A thicker shock confinement layer is necessary to ensure that a shock moving into the polymer does not reflect at the edge and return to the probed material before the end of the experiment. A 2 um thick confinement layer provides ~800 ps of delay. Second, as can be seen in Figure 4.9, application of this polymer layer caused significant loss of material, especially from thinner areas. This led to only small islands of material being available, far from a homogenous layer. It is unclear why material loss occurred as simple rinsing with water did not cause any noticeable change. It's possible that, as the HMX is not firmly adhered to the aluminum surface, the extremely viscous PVA solution simply sheared off thinner areas as it was flung off during the spin coating process. Third, as PVA was a solution in water, the polymer layer took several hours to cure. Delta HMX is not the thermodynamically stable polymorph at room temperature, so the PVA cannot be baked as usual. Instead it must be slowly cured under vacuum at room temperature. This is a problem both because delta HMX reverts back to beta HMX over a period of hours to days, and because delta HMX when exposed to water can undergo a conversion to gamma HMX.

To attempt to solve all these problems, many other polymer systems were tested. Most systems were unsuitable as the HMX must be completely insoluble in the solvent used. Various UV curable epoxies were tested and were promising, but were unable to be followed up on due to problems with the UV lamp. The best polymer conditions found were to use 20% PMMA in

chloroform. This consistently gave ~5um films with significantly less impact on the layer quality after spin coating. Unfortunately this extremely concentrated PMMA solution was not shelf stable and could not be stored more than a few days, while also requiring very large quantities and a saturated chloroform atmosphere in the spin coater to apply well. However, these were all possible and thus this was chosen as the polymer coating moving forwards.

After significantly increasing the concentration of the HMX solution, the coverage was quantified and the estimated distribution of % HMX coverage was determined as shown in Figure 4.10. The spread was enormous, and while some improvement was possible via averaging, it was still desired to reduce the spread somewhat. It was determined that both increasing the concentration and amount of HMX sprayed on improved the situation as can be seen in Figure 4.11, and time resolution was temporarily set aside to attempt to improve sample homogeneity. The concentration was increased again from 3mM to 50mM, and the total amount sprayed increased to an average thickness of 1 micron.

To test the variability in SFG signal as all of these parameters were varied, background scans were run repeatedly on the sample sample and the variance for each zone was compared. As can be seen in Figure 4.12, optimizing all these variables managed to bring the signal to ±10% from an initial ±25%. This was a significant improvement, but naturally still left something to be desired. However, as we were looking for intensity changes on the order of 50%, this level of variance was considered acceptable. Improving this further would likely require moving to a climate controlled area for spraying. It was also much later determined that for improved consistency in the polymorph distribution of the sprayed material, the samples should have been

baked at 200° C for 30 minutes. This treatment would also have been sufficient to convert beta

HMX layers deposited in any other fashion, such as dip coating, drop coating, or vapor deposition.

4.4 Results and Discussion:

Unfortunately, no change in the SFG signal was ever observed that could be clearly and

unambiguously assigned to the shock. As the shock wave passes through the HMX, the hope is

that we could observe some initiation event, which should take the form of irrecoverable loss of

SFG intensity, as well as possibly broadening and the appearance of new peaks representing new

species. If no initiation event occurs, it's possible that some changes would still occur due to

shifting of the molecular environment, but it is somewhat unclear. Unfortunately, as can be seen

in representative spectrum Figure 4.13, no noticeable shift or broadening was ever seen in the

SFG spectrum. These would have been the most unambiguous signs of a change.

While we can also look for major changes in SFG intensity, unfortunately there are several

confounding factors. As mentioned earlier, the SFG intensity varies by ±10% on the same sample.

This is most likely due to either small shifts in the position of the stage as it moves or slightly

wobbling in the stage itself, combined with the inhomogeneity in the sample layer. This means

that small shifts would be difficult to detect without significant averaging, itself difficult as the

shock destroys the sample. Furthermore, the laser destroys the aluminum substrate within the

first 100 ps, leading to a drastic loss of SFG signal as any SFG emission in that direction becomes

impossible to capture, and both probe beams no longer go through the material again. Based on

results from the monolayer shocking, we know that the shockwave takes around 60 ps to

propagate to the HMX substrate, and from there should be moving through the HMX for somewhat longer. Thus the loss of the aluminum is unfortunately right around the time that we would expect a reaction from the HMX, and thus makes it difficult to determine the origin of any intensity drops. An example of this can be seen in Figure 4.14, where by 100ps the intensity has dropped by more than 50% and never recovers.

The other major problem with looking for intensity changes is that, due to the thickness of the HMX sample, our time resolution is minimal. The shock wave moving through the material will compress the HMX, which is what is hoped will give a lowered SFG intensity. However, there is so much HMX that this drop and eventual recovery will be a much more gradual process, and thus not as easy to spot as simple sharp rises and falls. This also leads to a smaller drop as a percentage of total intensity, a problem as the run to run variance is already high. With some averaging, an effect was possibly seen as shown in Figure 4.15, but the effect is extremely minor and difficult to specifically assign to HMX being shocked rather than changes in the aluminum or positioning.

It is likely that several areas would need to be improved before the experiment could be successful. If the samples could be made much more reproducibly, even small changes could be detected. A pump pulse that was a few orders of magnitude more intense could be formed into a flat top and still have enough peak intensity to plausibly cause initiation, which would lead to larger effects in the sample area. A much thinner sample would also be necessary if any actual mechanistic information is going to be determined from the experiment.

4.5 References:

(1)   Asay, J. R. S., M., Eds *High-Pressure Shock Compression of Solids*; Springer-Verlag: New York, 1993.

(2)   Zel'dovich, Y. B. R., Y. P. *Physics of Shock Waves and High-Temperature Hydrodynamic Phenomena*; Academic Press: New York, 1966.

(3)   Hicks, D. G.; Boehly, T. R.; Celliers, P. M.; Eggert, J. H.; Moon, S. J.; Meyerhofer, D. D.; Collins, G. W. *Physical Review B* **2009**, *79*, 014112.

(4)   Boettger, J. C.; Wallace, D. C. *Physical Review B* **1997**, *55*, 2840.

(5)   Atou, T.; Kusaba, K.; Fukuoka, K.; Kikuchi, M.; Syono, Y. *Journal of Solid State Chemistry* **1990**, *89*, 378.

(6)   Patterson, J. E.; Dreger, Z. A.; Miao, M.; Gupta, Y. M. *The Journal of Physical Chemistry A* **2008**, *112*, 7374.

(7)   Winey, J. M.; Gupta, Y. M. *The Journal of Physical Chemistry A* **1997**, *101*, 9333.

(8)   Funk, D. J.; Moore, D. S.; McGrane, S. D.; Gahagan, K. T.; Reho, J. H.; Buelow, S. J.; Nicholson, J.; Fisher, G. L.; Rabie, R. L. *Thin Solid Films* **2004**, *453–454*, 542.

(9)   Graham, R. A. *Solids Under High-Pressure Shock Compression. Mechanics, Physics and Chemistry*; Springer-Verlag: New York, 1993.

(10)   Rygg, J. R.; Eggert, J. H.; Lazicki, A. E.; Coppari, F.; Hawreliak, J. A.; Hicks, D. G.; Smith, R. F.; Sorce, C. M.; Uphaus, T. M.; Yaakobi, B.; Collins, G. W. *Review of Scientific Instruments* **2012**, *83*, 113904.

(11)   Nagao, H.; Nakamura, K. G.; Kondo, K.; Ozaki, N.; Takamatsu, K.; Ono, T.; Shiota, T.; Ichinose, D.; Tanaka, K. A.; Wakabayashi, K.; Okada, K.; Yoshida, M.; Nakai, M.; Nagai, K.; Shigemori, K.; Sakaiya, T.; Otani, K. *Physics of Plasmas* **2006**, *13*, 052705.

(12)   Bolme, C. A.; McGrane, S. D.; Moore, D. S.; Funk, D. J. *Journal of Applied Physics* **2007**, *102*, 033513.

(13)   Dlott, D. D. *Accounts of Chemical Research* **2000**, *33*, 37.

(14)   Dlott, D. D.; Hambir, S.; Franken, J. *The Journal of Physical Chemistry B* **1998**, *102*, 2121.

(15)   Gahagan, K. T.; Moore, D. S.; Funk, D. J.; Rabie, R. L.; Buelow, S. J.; Nicholson, J. W. *Physical Review Letters* **2000**, *85*, 3205.

(16)   Crowhurst, J. C.; Armstrong, M. R.; Knight, K. B.; Zaug, J. M.; Behymer, E. M. *Physical Review Letters* **2011**, *107*, 144302.

(17)   Holian, B. L. *Shock Waves* **2004**, *13*, 489.

(18)   Strachan, A.; van Duin, A. C. T.; Chakraborty, D.; Dasgupta, S.; Goddard, W. A. *Physical Review Letters* **2003**, *91*, 098301.

(19)   Nomura, K.-i.; Kalia, R. K.; Nakano, A.; Vashishta, P.; van Duin, A. C. T.; Goddard, W. A. *Physical Review Letters* **2007**, *99*, 148303.

(20)   Wood, M. A.; van Duin, A. C. T.; Strachan, A. *The Journal of Physical Chemistry A* **2014**, *118*, 885.

(21)   Gustavsen, R. L.; Sheffield, S. A.; Alcon, R. R. *AIP Conference Proceedings* **1998**, *429*, 739.

(22)   Switzer, L. L.; Vandersall, K. S.; Chidester, S. K.; Greenwood, D. W.; Tarver, C. M. In *AIP Conference Proceedings*; IOP INSTITUTE OF PHYSICS PUBLISHING LTD: 2004; Vol. 706, p 1045.

(23)   Patterson, J. E.; Lagutchev, A.; Huang, W.; Dlott, D. D. *Physical Review Letters* **2005**, *94*, 015501.

(24)   Lagutchev, A. S.; Patterson, J. E.; Huang, W.; Dlott, D. D. *The Journal of Physical Chemistry B* **2005**, *109*, 5033.

(25)   Patterson, J. E.; Dlott, D. D. *The Journal of Physical Chemistry B* **2005**, *109*, 5045.

(26)   Berg, C.; Lagutchev, A.; Fu, Y.; Dlott, D. *AIP Conference Proceedings* **2012**, *1426*, 1573.

(27)   Marsh, S. P. *LASL shock Hugoniot data*; Univ of California Press, 1980; Vol. 5.

(28)   Fu, Y.; Friedman, E. A.; Brown, K. E.; Dlott, D. D. *Chemical Physics Letters* **2011**, *501*, 369.

(29)   Berg, C.; Lagutchev, A.; Fu, Y.; Dlott, D.; Elert, M. L.; Buttler, W. T.; Borg, J. P.; Jordan, J. L.; Vogler, T. J. In *AIP Conference Proceedings-American Institute of Physics* 2012; Vol. 1426, p 1573.

(30)   Cady, H. H. S., Louis C. *LAMS* **1962**, *LAMS-2652*.

(31)   Nafday, O.; emsp14; Pitchimani, R.; Weeks, B.; emsp14; Haaheim, J. *Propellants Explosives Pyrotechnics* **2006**, *31*, 376.

4.6 Figures:
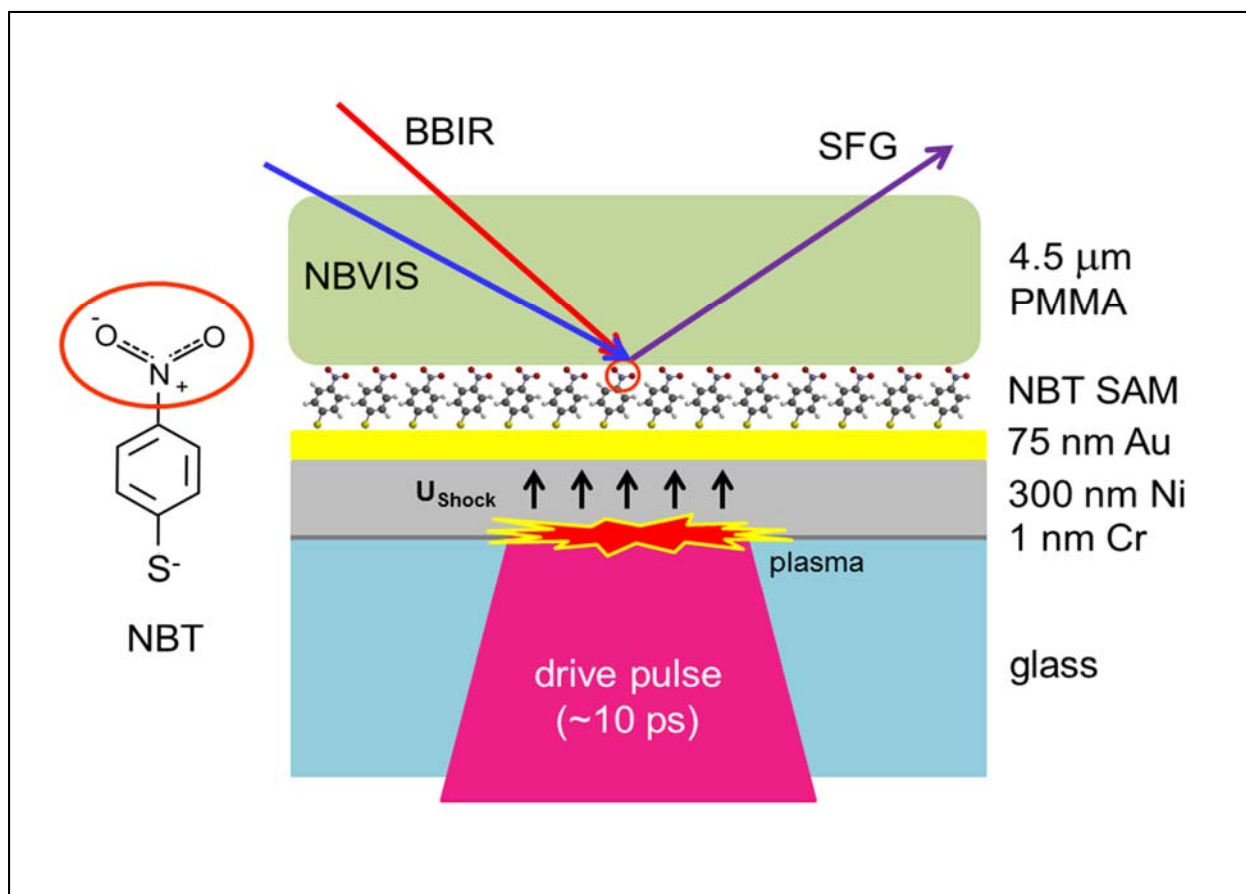
Figure 4.1. A diagram of the sample used for shock compression of monolayers
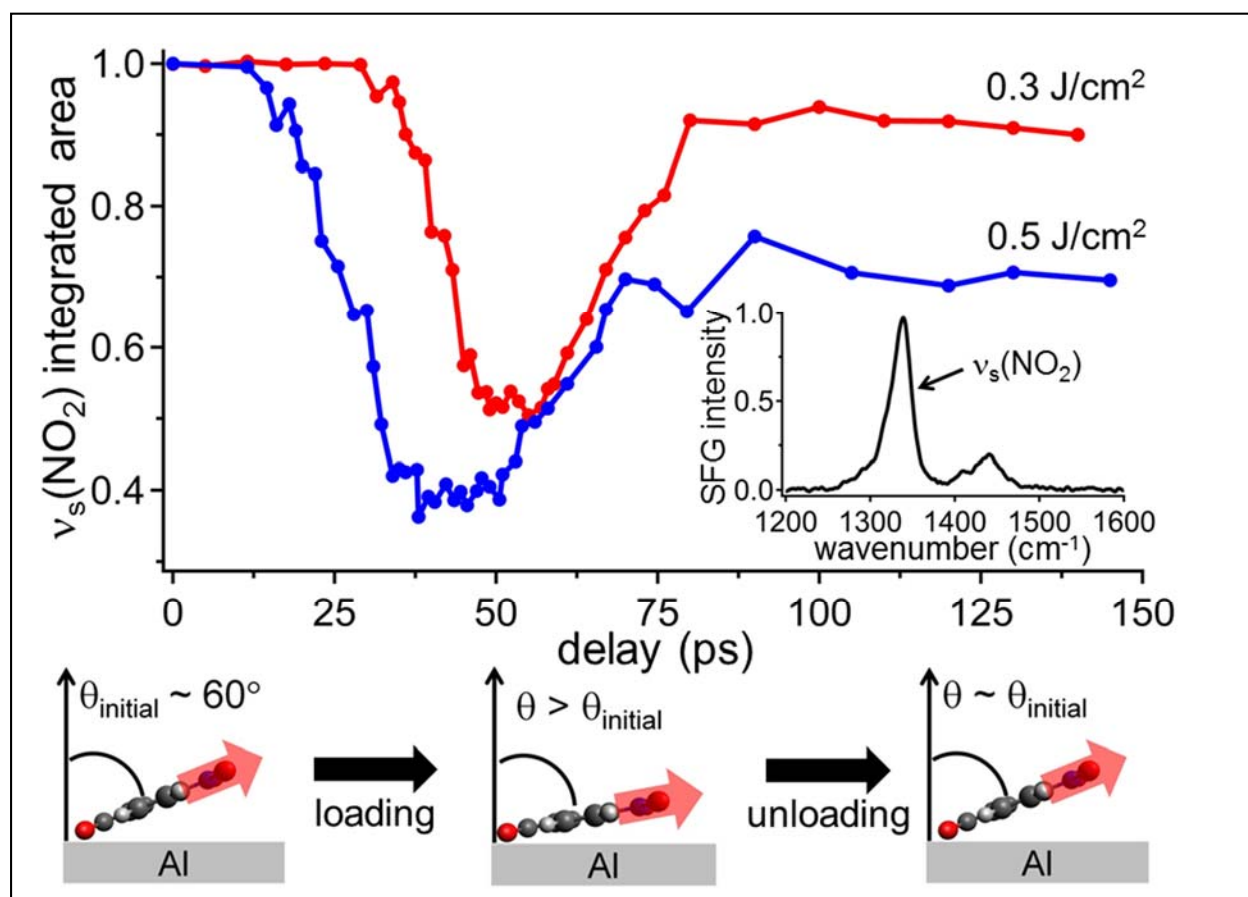
Figure 4.2. Time resolved transients of the integrated SFG intensity for the symmetric nitro stretch (inset) of nitrobenzoic acid. Shock causes tilting of the molecules towards the surface, which then recovers over tends of picoseconds. At higher laser fluences, recovery is incomplete.
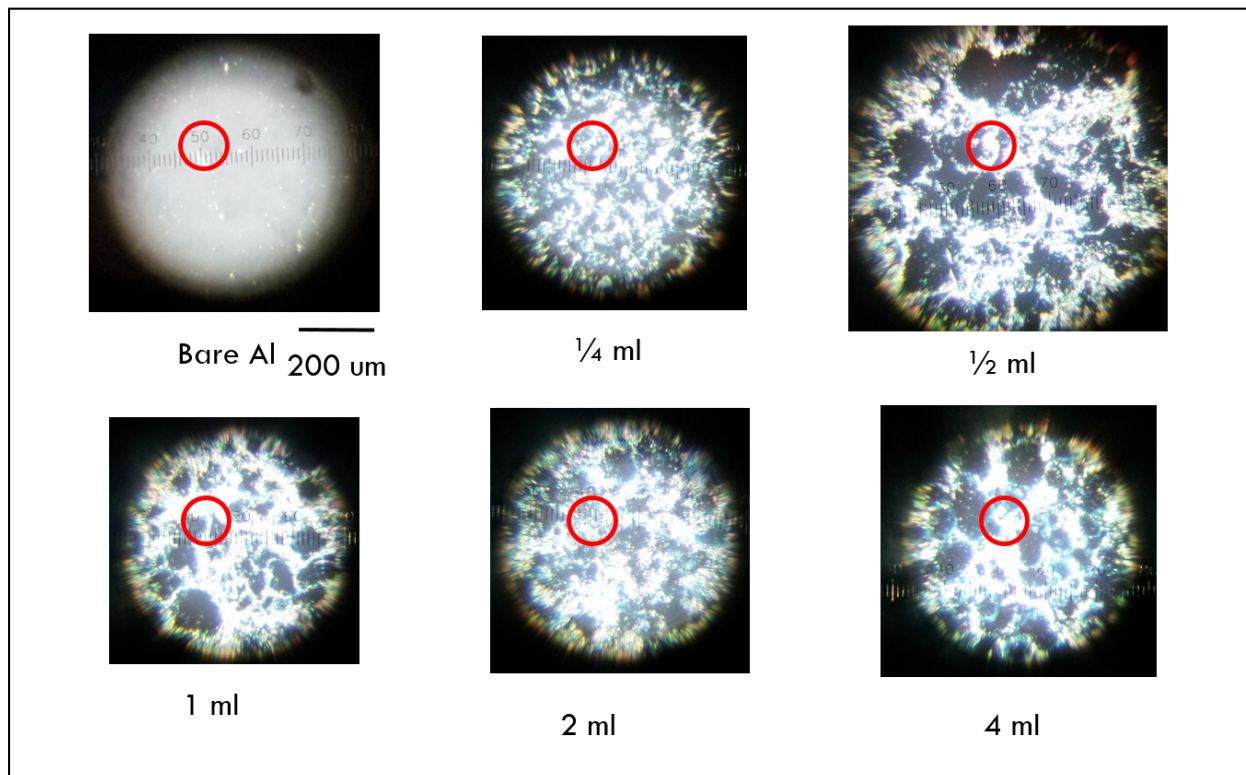
Unheated

250 um   Heated to 35 C
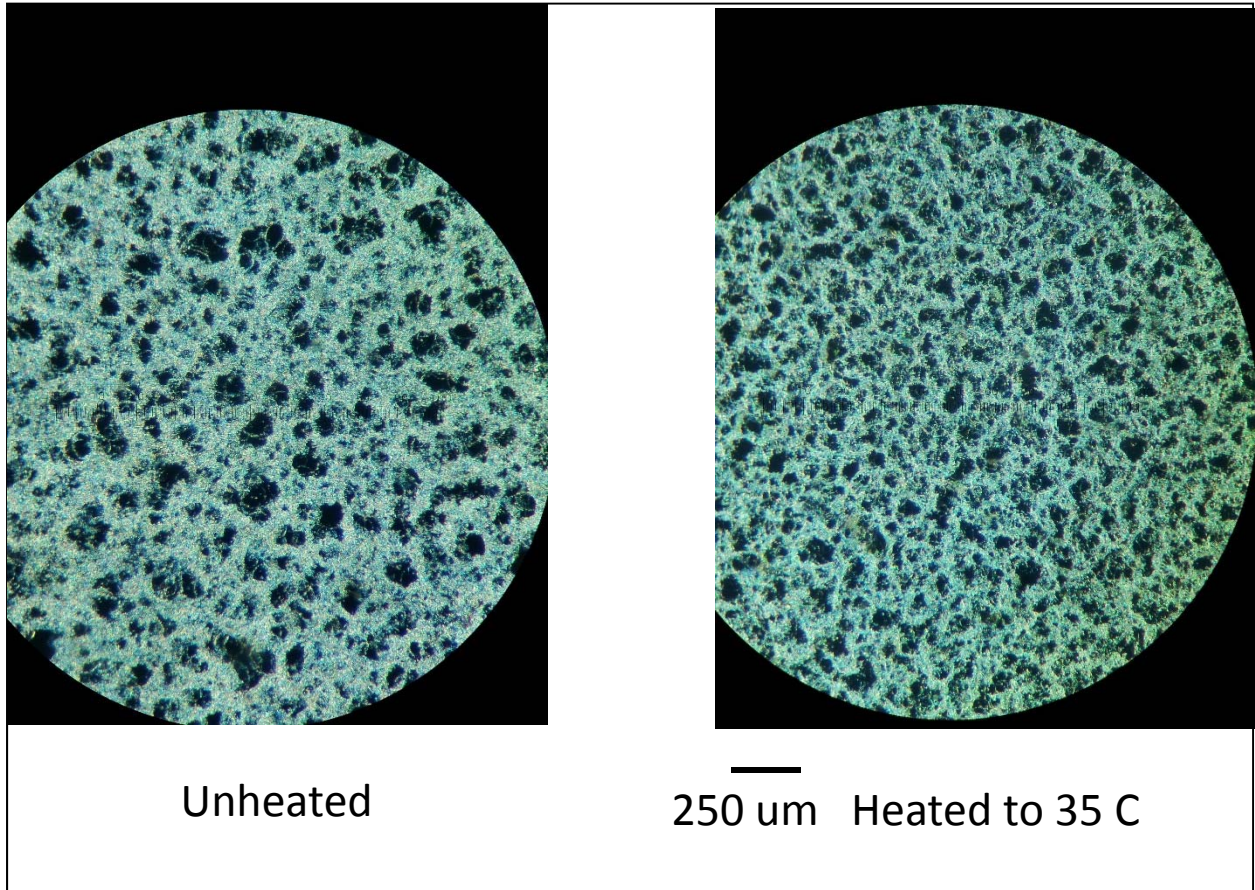
Figure 4.3. Light microscope images of spray coated layers of HMX on substrates that were either at room temperature or at 35 C during deposition.
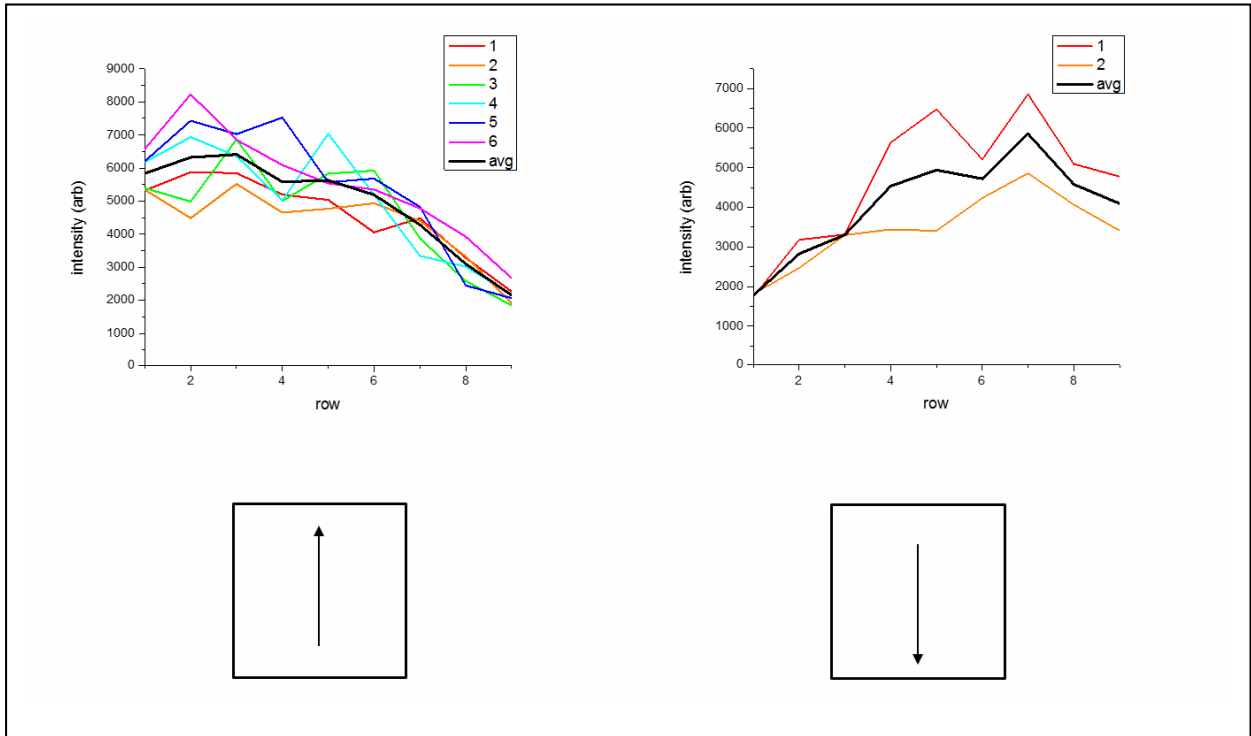
Figure 4.4. SFG intensity for 9 separate bands on the sample, going either bottom to top (left) or top to bottom (right)
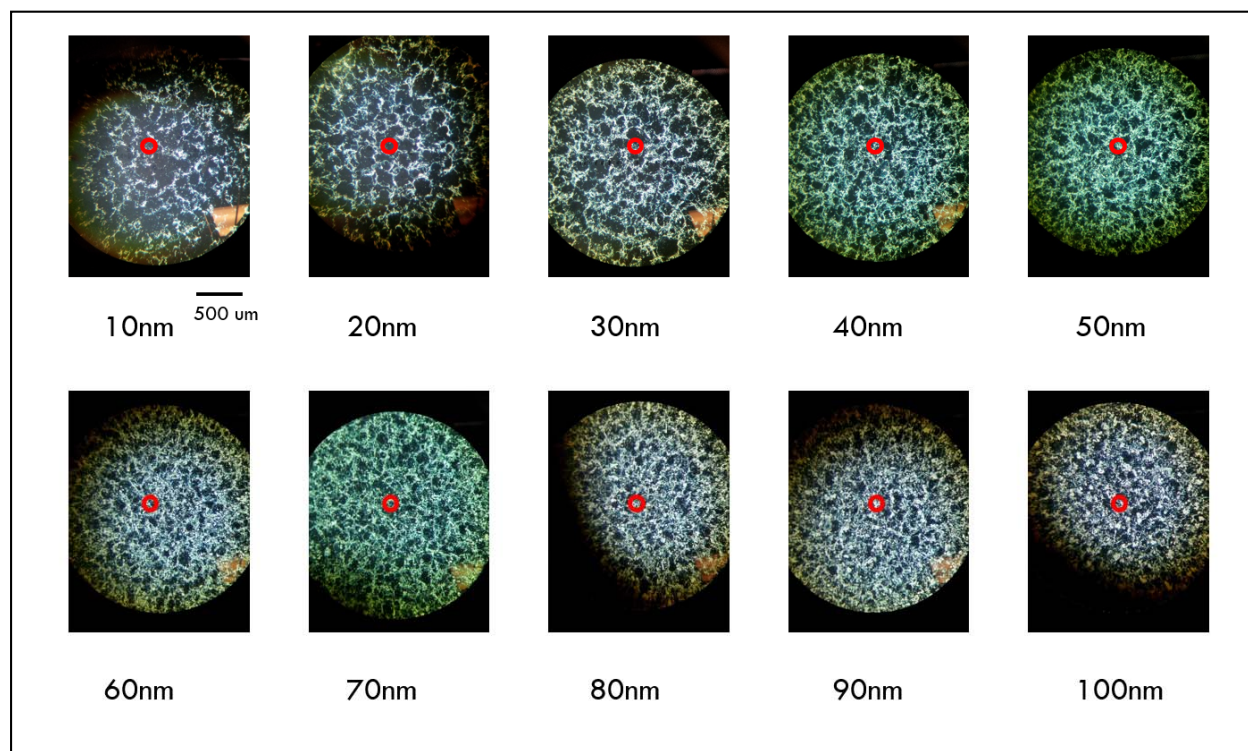
Figure 4.5. Light microscope images of spray coated HMX from a solution made from the listed volume of acetone with a fixed amount of HMX. The lighter material is the HMX. The size of the area probed in the experiment is represented with a red circle
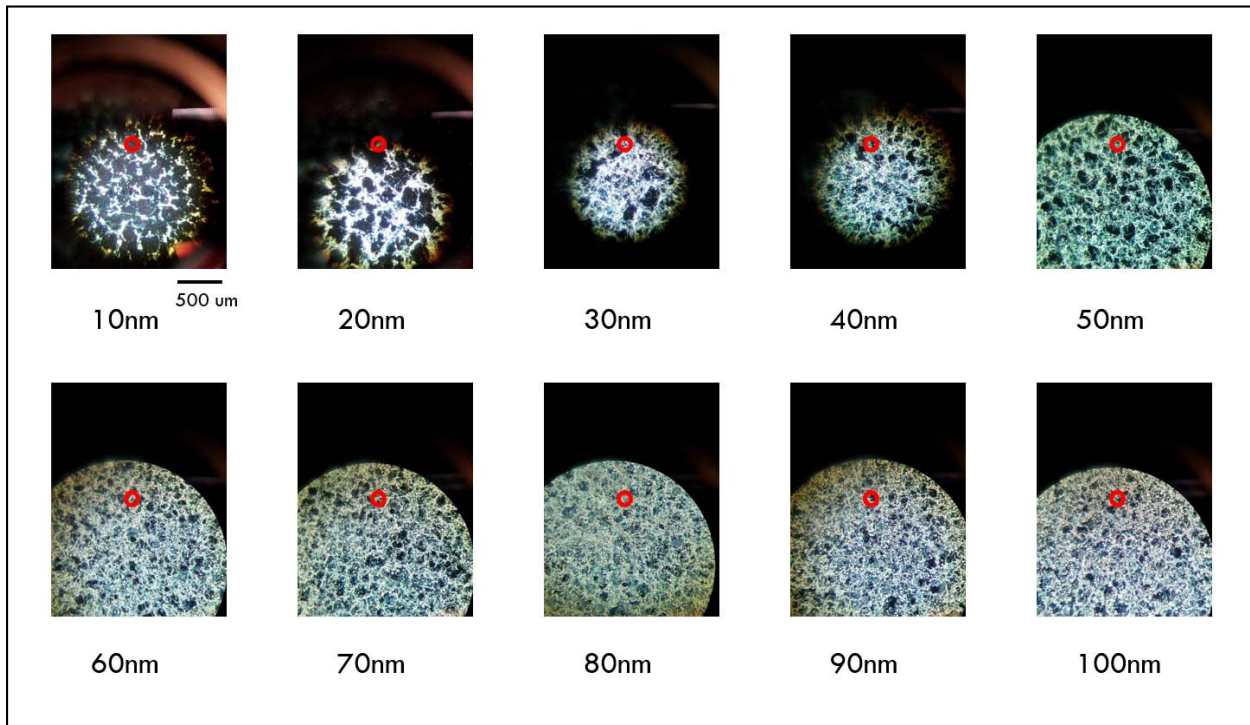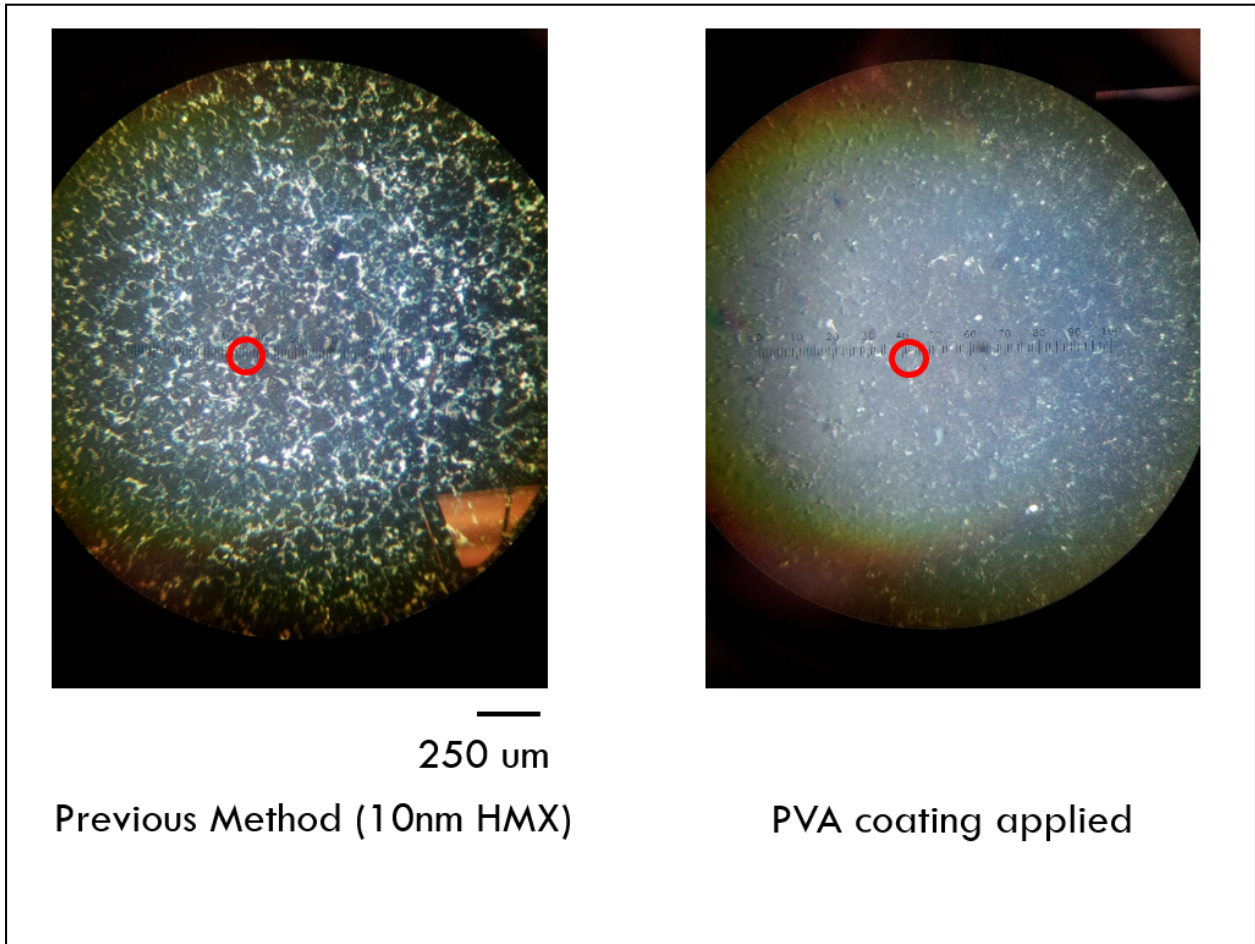
Figure 4.6. Light microscope images of spray coated HMX with the listed average thickness, sprayed directly onto a clean aluminum surface. The size of the area probed in the experiment is represented with a red circle.

10nm 500 um 20nm 30nm 40nm 50nm

60nm 70nm 80nm 90nm 100nm
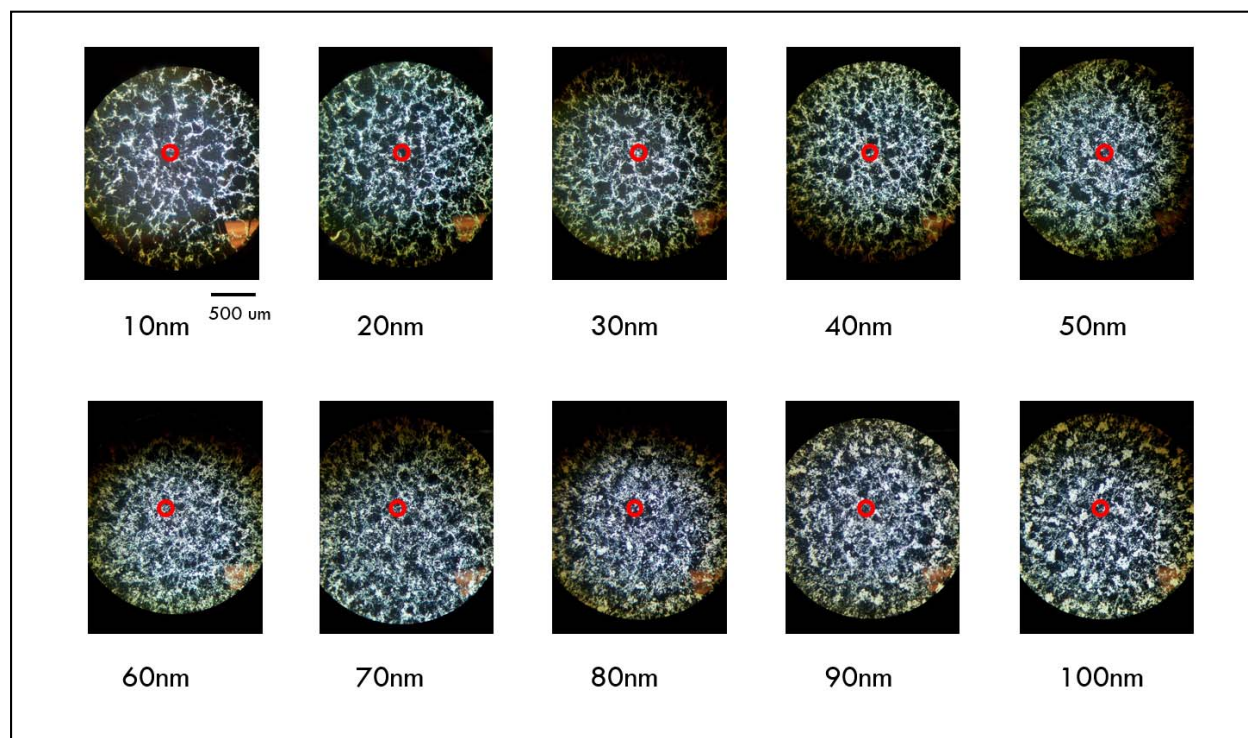
Figure 4.7. Light microscope images of spray coated HMX with the listed average thickness, sprayed directly onto an aluminum surface with a nitrobenzoic acid monolayer applied. The size of the area probed in the experiment is represented with a red circle.
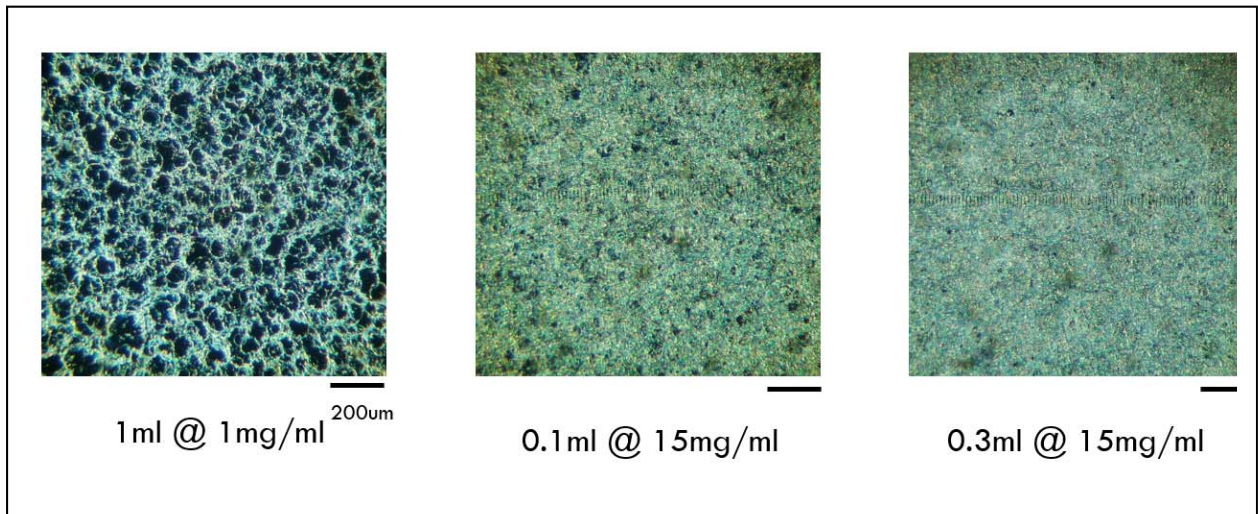
Figure 4.8. Light microscope images of spray coated HMX with the listed average thickness, sprayed directly onto an aluminum surface with a terephthalic acid monolayer applied. The size of the area probed in the experiment is represented with a red circle.

250 um

Previous Method (10nm HMX)   PVA coating applied

Figure 4.9. Light microscope images of spray coated HMX with the listed average thickness (left), and the same sample after the PVA coating has been applied (right)
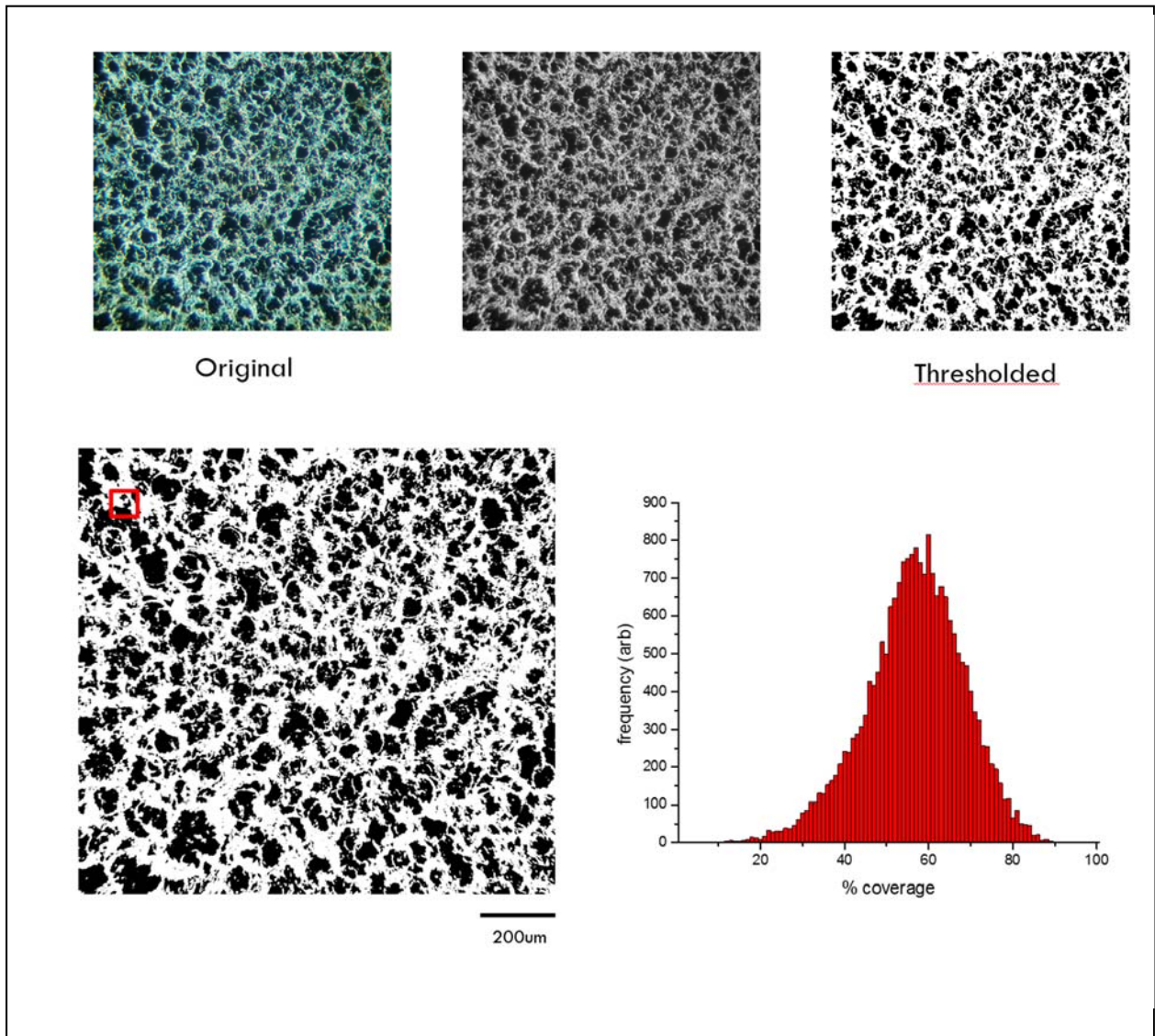
Figure 4.10. A figure of the process for determining the distribution of HMX coverage for 50um squares over the entire sample. The image is thresholded and approximated as each pixel having either no HMX or a constant amount of HMX. The distribution of coverage for the sample shown is shown in the bottom right
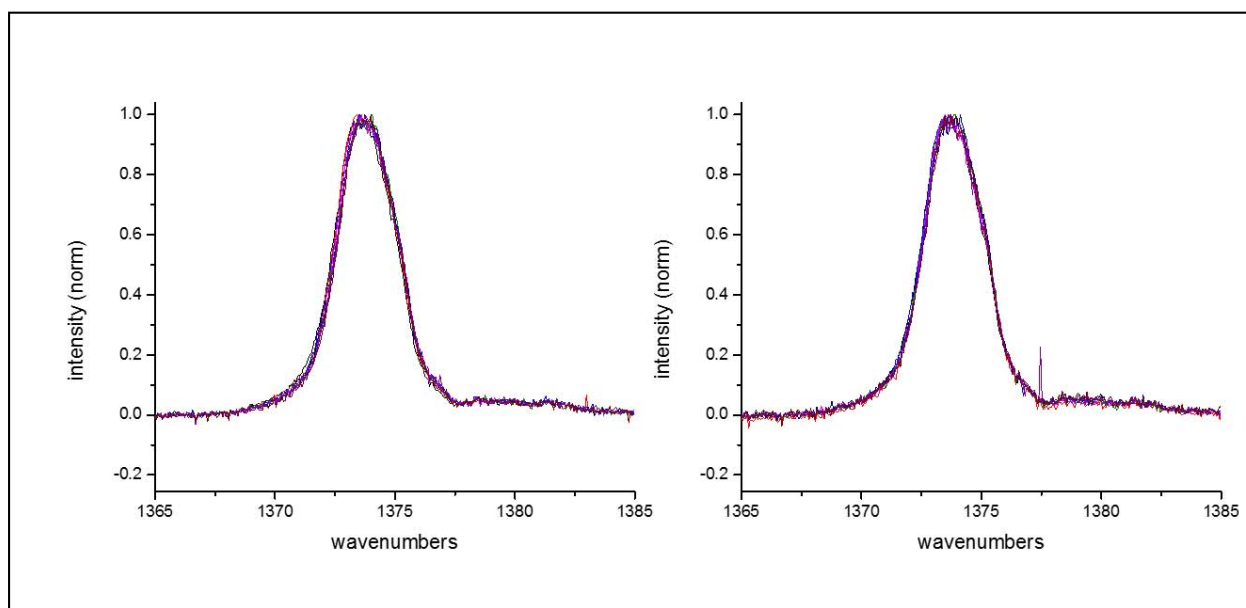
Figure 4.11. Light microscope images of spray coated HMX with the listed volume and concentrations of HMX solution in acetone.
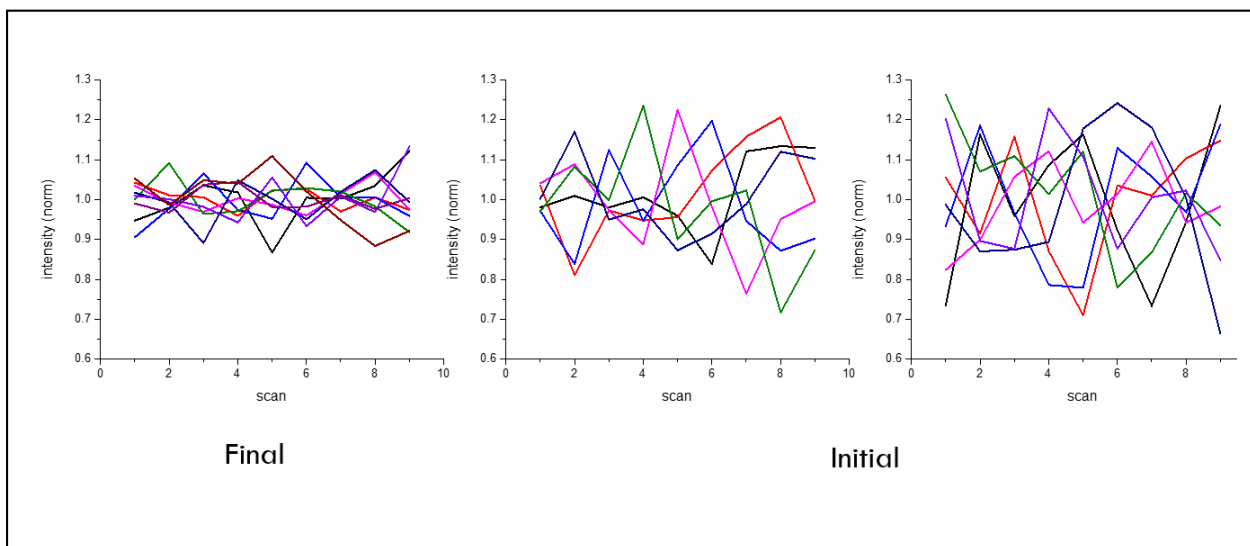
Figure 4.12. Deviation from the average for each of 9 slices on a sample slide. The left represents the final optimized sample preparation conditions, which the middle and right are representative scans with initial conditions.
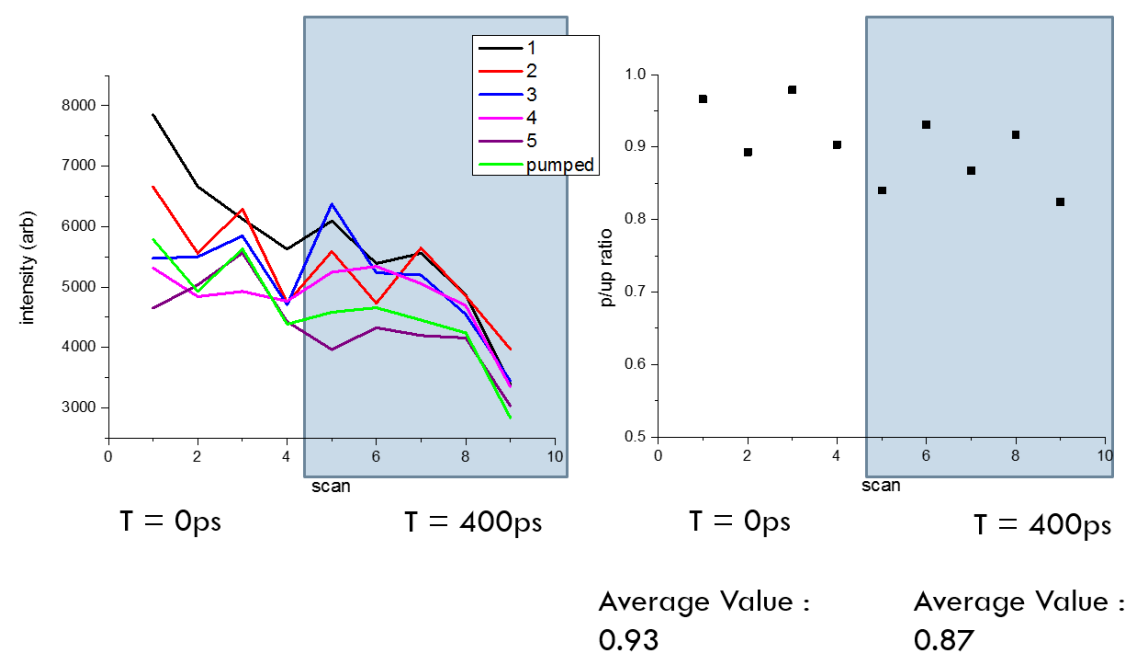
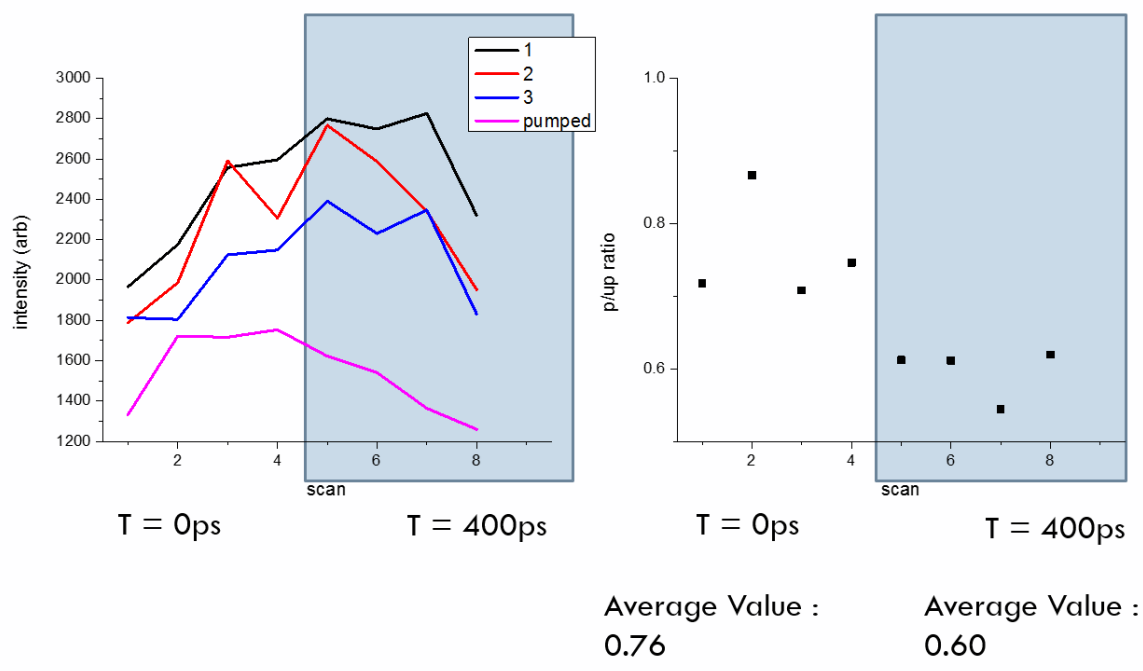**Figure 4.13.** SFG spectra of the nitro stretch. The left has 9 spectra, none of which are taken during shock. The right has 5 spectra taken during the time period the shockwave is expected to be in the HMX. No difference can be seen.
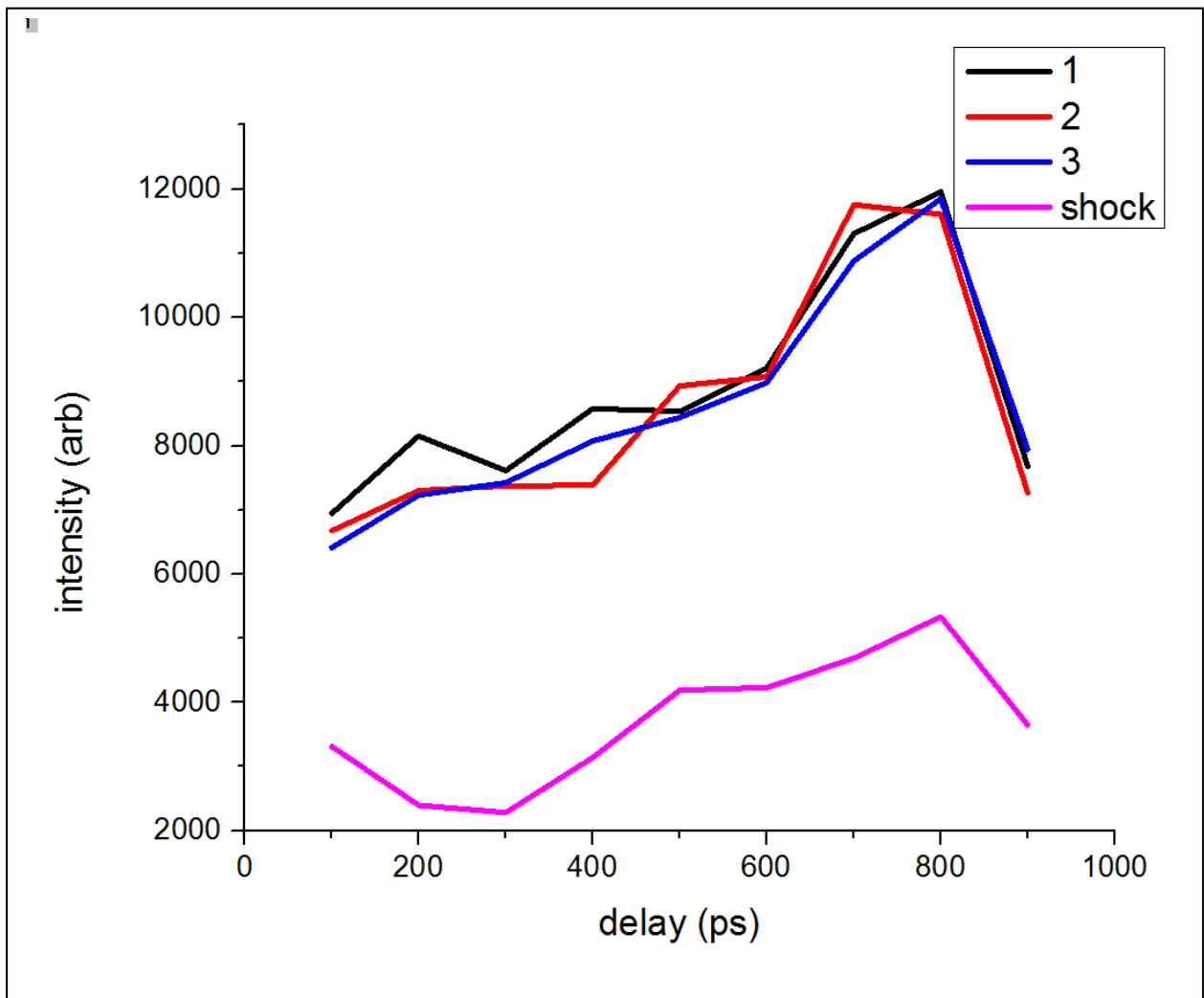
Figure 4.14. A representative scan showing 3 sets of intensities before shocking and one during. The intensity loss from losing the aluminum is large and occurs by 100 ps

T = 0ps   T = 400ps   T = 0ps   T = 400ps

Average Value :
0.76

Average Value :
0.60

T = 0ps   T = 400ps   T = 0ps   T = 400ps

Average Value :
0.93

Average Value :
0.87

Figure 4.15. Four separate sets of scans with the first four points at t=0 and the next five points at t = 400ps. The hope is that any drops due to the HMX being shocked specifically could be detected via averaging.

T = 0ps   T = 400ps   T = 0ps   T = 400ps

Average Value :   Average Value :
0.98   0.99

T = 0ps   T = 400ps   T = 0ps   T = 400ps

Average Value :   Average Value :
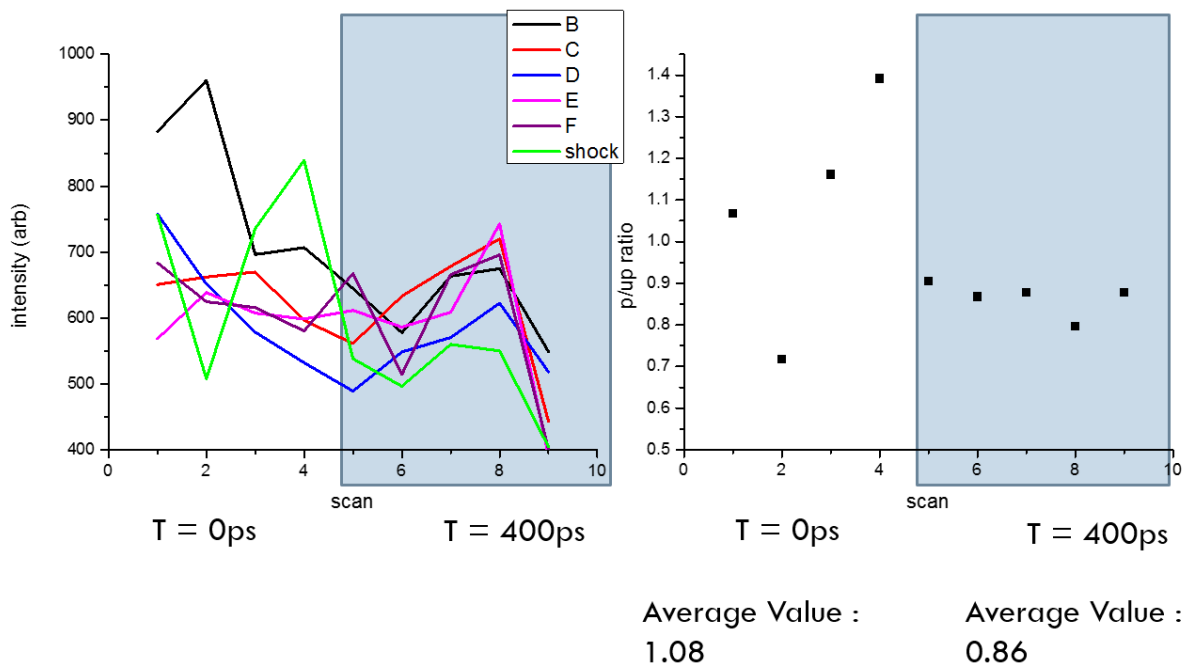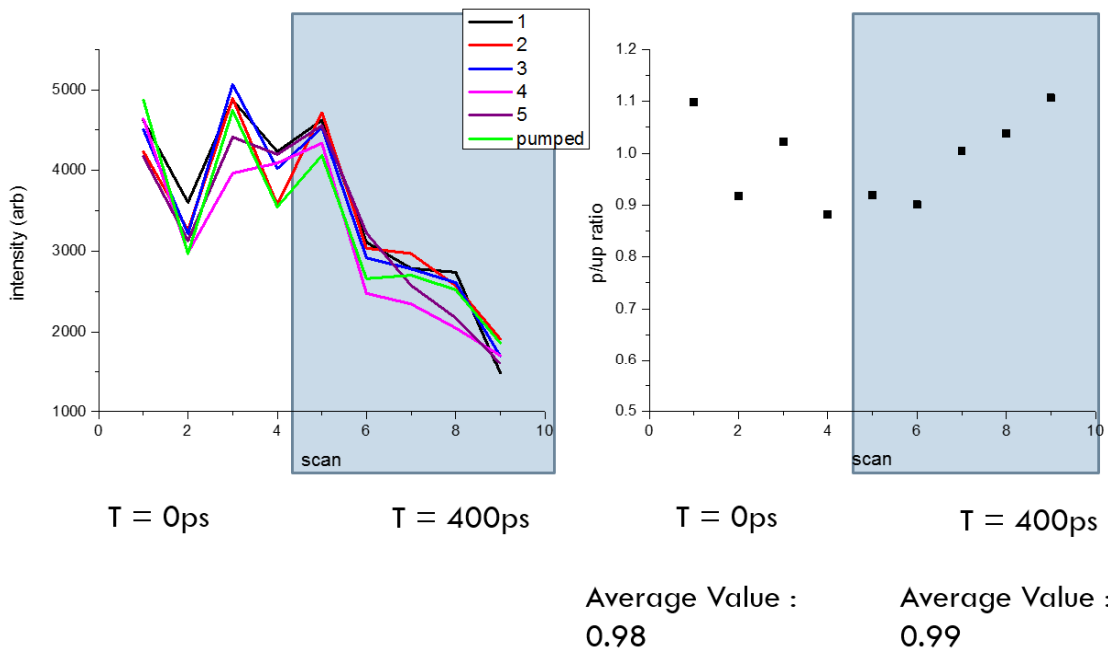1.08   0.86

Figure 4.15. (cont.)

Chapter 5: Flyer Driven Shock Initiation of Molecular Explosives

5.1 Introduction:

It is vitally important to understand the sensitivity of an explosive before it can be used with confidence, but there are many kinds of sensitivity, all of which are at best poorly correlated with each other. While we have convenient ways of measuring some types of sensitivities, such as impact[1] and friction,[2] shock sensitivity is significantly more difficult. Currently, shock sensitivity is best measured using a gas gun[3], an immense instrument with terrible throughput requiring grams of material to test. However, the flyer plate system in use by the Dlott group potentially allows for hundreds of shots a minute instead of a few shots a day, and requires only milligrams.

Furthermore, the flyer plate system has been used to study the first nanoseconds after shock compression for HMX.[4] Interesting new phenomena have been observed using an emission spectrometer, and so it was of great interest how the completely different microstructure of spray coated HMX would behave. Similarly, being able to use the emission spectrometer to look for differences in the shock compression of beta and delta HMX is of great interest. There have been models put forth that involve an initial conversion of beta to delta HMX[5-7] before ignition occurs, but fairly little experimental evidence.

Thus the goal of this study twofold. First is to use the flyer plate system and attempt to determine the difference in shock sensitivity between delta and beta HMX as a test system. A tabletop system capable of determining the relative shock sensitivities of two materials could be immensely valuable to the field, especially in the testing of newly made materials. Second is to

directly compare the shock compression of beta and delta HMX. This could provide useful information about the processes that occur before HMX detonation, allowing a better understanding of the mechanisms involved.

5.2 Previous Studies on Beta and Delta HMX:

There have been many studies on the relative sensitivity of HMX polymorphs, and a few of the most relevant will be highlighted here. Cady and Smith published one of the earliest accessible works[8] aimed at thoroughly determining the relative stabilities of the HMX polymorphs using ERL Type 12 and 12B machines.[1] The apparatus is a standard drop hammer design, using a microphone to detect initiation events. The Type 12 apparatus has the sample sitting on fine sandpaper, while the Type 12B apparatus has the material sit directly on the anvil. They find that using this apparatus, the samples of delta HMX tested were in every case more sensitive than the beta HMX control. This held true for samples of delta HMX contaminated with up to 40% beta HMX, though there was no clear correlation between composition and sensitivity. The difference in sensitivities was significantly larger for experiments run on the Type 12B apparatus, no explanation was given for this phenomenon.

Herrmann et al[9] determined friction sensitivities of both ground and unground samples of HMX polymorphs using a BAM apparatus.[2] The apparatus involves grinding the material with a specified load on the sample, and then looking for explosions, sparks, and other events indicating initiation. They were unable to detect any difference between ground and unground

samples, and found that delta HMX had significantly higher friction sensitivity compared to beta HMX. No testing of mixtures of polymorphs was done.

Peterson et al[10] using both the Type 12 apparatus and the BAM apparatus reconfirm the preceding findings, and also show that beta HMX that has been converted to delta HMX via heating and then allowed to revert over time has essentially the same sensitivity as the initial material. Asay et al[7] use a gas gun and samples of PBX 9501 (95% by volume HMX in a bimodal distribution of ~120 and 30um diameter particles formulated with Estane and a 50/50 eutectic mixture of bis(2,2-dinitropropyl) acetal and bis(2,2-dinitropropyl) formal) that have been converted to delta and then converted back to confirm that shock sensitivity for pristine beta and reverted beta are essentially the same. They make no statement on the relative sensitivities of the two polymorphs.

Thus combined, it's known that beta HMX is generally more sensitive than delta HMX when it comes to impact sensitivity and friction sensitivity, but shock sensitivity is a little less well studied. There is significant evidence that the approach taken here of converting HMX to delta and then back to beta creates a material that does not significantly differ from pristine beta HMX in shock, impact, or friction sensitivity. Thus our comparisons should be valid for beta HMX in general rather than our reconverted material specifically.

5.3 Sample Design:

The original samples were thin films of HMX spray coated onto glass in the same fashion as the laser driven shock samples, but without a metal layer and with larger glass substrates for

convenience. However, several problems arose that were not present with laser driven shocks. First, it was found at flyer speeds of greater than ~1 km/s, the flyers started damaging sample areas adjacent to the ones being shot. The cause of this is unclear as it also occurs in the control samples, but likely involve shockwaves traveling laterally through the material. A mask was used during the spray coating process to separate the sample into individual 3mm diameter circles evenly spaced on the substrate, which was sufficient to isolate the shots.

Second, while the laser driven shocks were simply looking to observe any initiation, in this experiment sample composition was of vital importance, as it has been shown that the specific mix of polymorphs can affect sensitivity.[8] Thus as we wish to compare delta and beta HMX, the samples need to be as close to pure single polymorph HMX as possible. The spray coated samples have been shown to be primarily delta,[11] but variations are possible depending on temperature and humidity, so samples were baked to give as close to 100% delta as possible. The conversion back to beta was achieved by exposing the sample to solvent vapors, but the kinetics of the conversion are strongly dependent on temperature and humidity, and so the sample was simply monitored via FTIR to determine when conversion had fully occurred.

As the desired time resolution was now on the scale of nanoseconds to tens of nanoseconds, the sample could also be much thicker, thus providing significantly more signal. As such, the sample here is on average 10 um thick, and could be thicker without any negative impact. However, attempts to spray coat even thicker layers failed, as HMX tended to aggregate into tall crystals rather than forming a thicker uniform layer. While the samples will likely still be homogenous on the flyer plate length scale, there is a definitely possibility that a flyer plate hitting these tall crystals before the surface would change something about the impact or

subsequent reactions. As the polymorph mix after deposition is irrelevant due to subsequent heat treatment, it is likely that some other coating technique will be required to form high quality thicker samples.

Outside of these specific changes made to accommodate the spray coated HMX, the sample chamber and laser system are identical to those used for flyer plate impacts on powdered HMX,[12] allowing for somewhat more direct comparisons between those and these spray coated layers.

5.4 Results and Discussion:

Figure 5.1 shows the radiance integrated over the first 100ns after impact for delta, and beta HMX as well as the oxalic acid control for a variety of flyer impact speeds. Each red bar represents an individual shot, and empty spaces between bars represent instances where noise caused the integrated radiance to go negative. In some instances, fewer shots were taken at a velocity and thus fewer bars are present. General trends can be seen from this, but for a clearer picture, shots at several representative speeds were averaged, and the results can be seen in Figure 5.2. This allows us to easily compare radiances at specific impact velocities against the control. It can be clearly seen that at 0.38 km/s neither HMX bar has significantly more intensity than the control, but at 0.53 km/s the delta HMX has an order of magnitude more radiance compared to both the control and beta HMX. At the even higher velocity of 0.71 km/s, both HMX polymorphs have comparable radiance, and both are many orders of magnitude above the control.

Figure 5.3 shows the time resolved radiance and average temperature for several representative impact velocities for both delta (black) and beta (red) HMX. The methodology for graybody temperature modeling have been described previously.[10] Figure 5.4 shows a representative time resolved spectrum, with example temperature fits for the events at 10 ns and 100ns. We can see that the initial intense peak lasts only tens of nanoseconds, which is why the first 100 ns are used to judge initiation. At higher speeds, another event can be observed at around 100-200ns. However, as we can see from the figure, the temperatures of the second event are much lower than that of our initiation event, and as such may be attributable to some other follow up event.

Unfortunately the signal to noise ratio at lower impact velocities is too poor to fit well, so temperatures are not available for velocities below 0.71 km/s. It can be seen from the temperature plots that there is a significant event occurring around 10 us which causes a jump in temperature for both delta and beta HMX, however this event appears to disappear as velocities increase. No temperatures were able to be determined for the control samples.

Emission spectra were collected from spray coated layers of two different polymorphs of HMX as well as a control material as a function of flyer velocity, which ranged from 0.15 to 2.65 km/s. By examining the integrated radiance over the first 100 ns at a variety of speeds and comparing values to the control shots, it can be determined how much of the total radiance is due to the HMX. When there is significantly higher radiance from the HMX compared to the control values, it is likely some initiation event occurred in the HMX. As can be seen in Figure 5.2, at very low speeds (0.38 km/s), both polymorphs of HMX are within error of the control, so likely no initiation is occurring. At a higher speed (0.53 km/s), the delta-HMX has radiance almost an

78

order of magnitude above the control, while the beta-HMX is slightly below but still within error of the control. This is in line with prior work on the relative sensitivities of HMX polymorphs.[7-9,13] At even higher speeds (0.71 km/s), clearly both HMX polymorphs have undergone initiation with radiances that are within error of each other and over an order of magnitude above the control.

Temperatures were able to be determined for velocities of 0.71 km/s or higher, and are fairly similar to measured earlier by the Dlott group,[2] with an initial temperature spike of around 6000° and a rapid dropoff, with another feature in the microsecond region. An interesting difference can be seen in the temperature plot for 1.0 km/s. There is also a significant difference in the magnitude of the microsecond temperature jump between delta and beta, with beta having a temperature jump almost 600° higher than delta. It is possible that this is due to the difference in sensitivities causing less material to be consumed in the early initiation event, thus leaving more available to react later. This is also borne out by the lack of any noticeable microsecond event at velocities of 1.25km/s and higher, perhaps due to a near complete reaction of the material in the initial burst.

5.5 References:

(1)   Simpson, L. R.; Foltz, M. F. *LLNL small-scale drop-hammer impact sensitivity test*, Lawrence Livermore National Lab., CA (United States), 1995.

(2)   Simpson, L. R.; Foltz, M. F. *LLNL Small-Scale Friction Sensitivity (BAM) Test*, Lawrence Livermore National Lab., CA (United States), 1996.

(3)   Mitchell, A.; Nellis, W. *Review of scientific instruments* **1981**, *52*, 347.

(4)   Bassett, W. P.; Dlott, D. D. *Journal of Applied Physics* **2016**, *119*, 225103.

(5)   Henson, B. F.; Asay, B. W.; Smilowitz, L. B.; Dickson, P. In *AIP Conference Proceedings*; IOP INSTITUTE OF PHYSICS PUBLISHING LTD: 2002, p 1069.

(6)   Karpowicz, R. J.; Brill, T. *Aiaa Journal* **1982**, *20*, 1586.

(7)   Asay, B. W.; Henson, B. F.; Smilowitz, L. B.; Dickson, P. M. *Journal of Energetic Materials* **2003**, *21*, 223.

(8)   Cady, H. H. S., Louis C. *LAMS* **1962**, *LAMS-2652*.

(9)   Herrmann, M.; Engel, W.; Eisenreich, N. *Propellants, Explosives, Pyrotechnics* **1992**, *17*, 190.

(10)   Peterson, P. D.; Lee, K. Y.; Moore, D. S.; Scharff, R. J.; Avilucea, G. R. *AIP Conference Proceedings* **2007**, *955*, 987.

(11)   Surber, E.; Lozano, A.; Lagutchev, A.; Kim, H.; Dlott, D. D. *The Journal of Physical Chemistry C* **2007**, *111*, 2235.

(12)   Banishev, A. A.; Shaw, W. L.; Bassett, W. P.; Dlott, D. D. *Journal of Dynamic Behavior of Materials* **2016**, *2*, 194.

(13)   Kohno, Y.; Maekawa, K.; Tsuchioka, T.; Hashizume, T.; Imamura, A. *Combustion and Flame* **1994**, *96*, 343.

5.6 Figures:
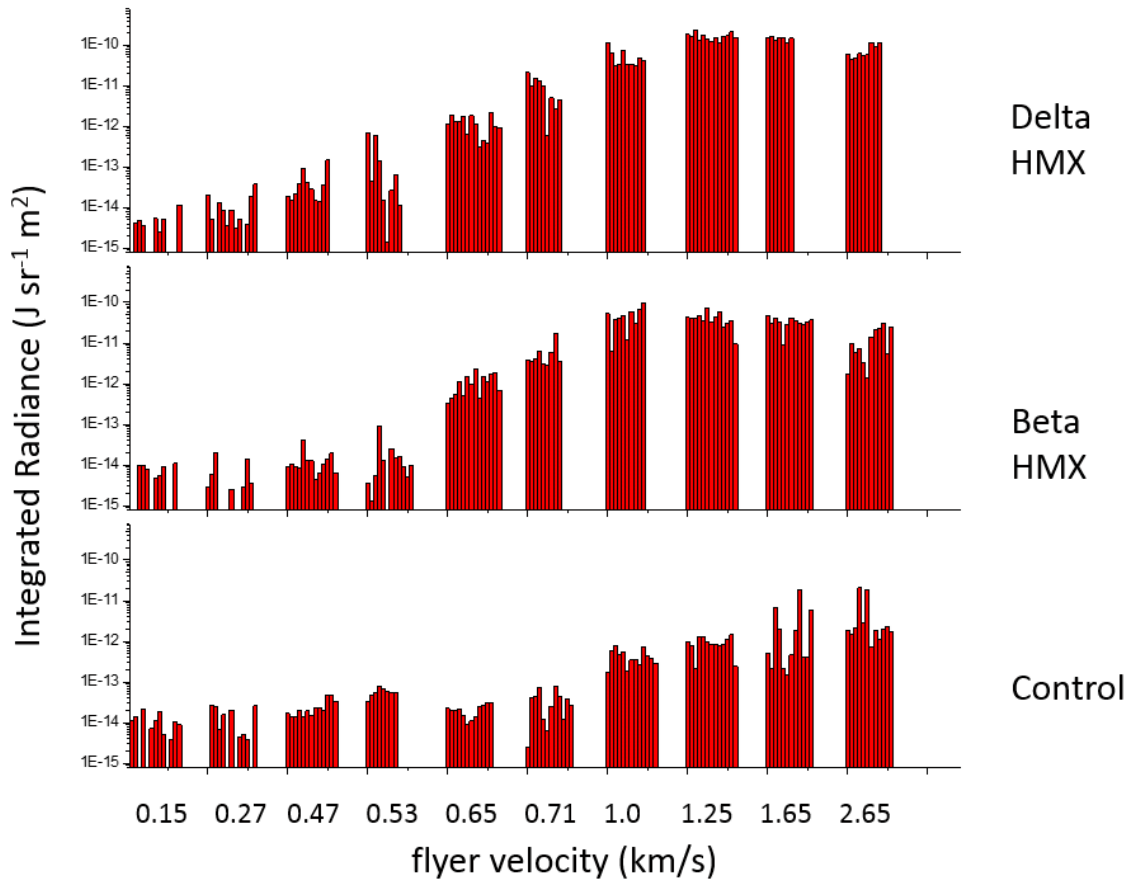
Figure 5.1. Radiance integrated over the first 100ns after flyer impact for spray coated layers of δ-HMX, β-HMX, and oxalic acid as a control.
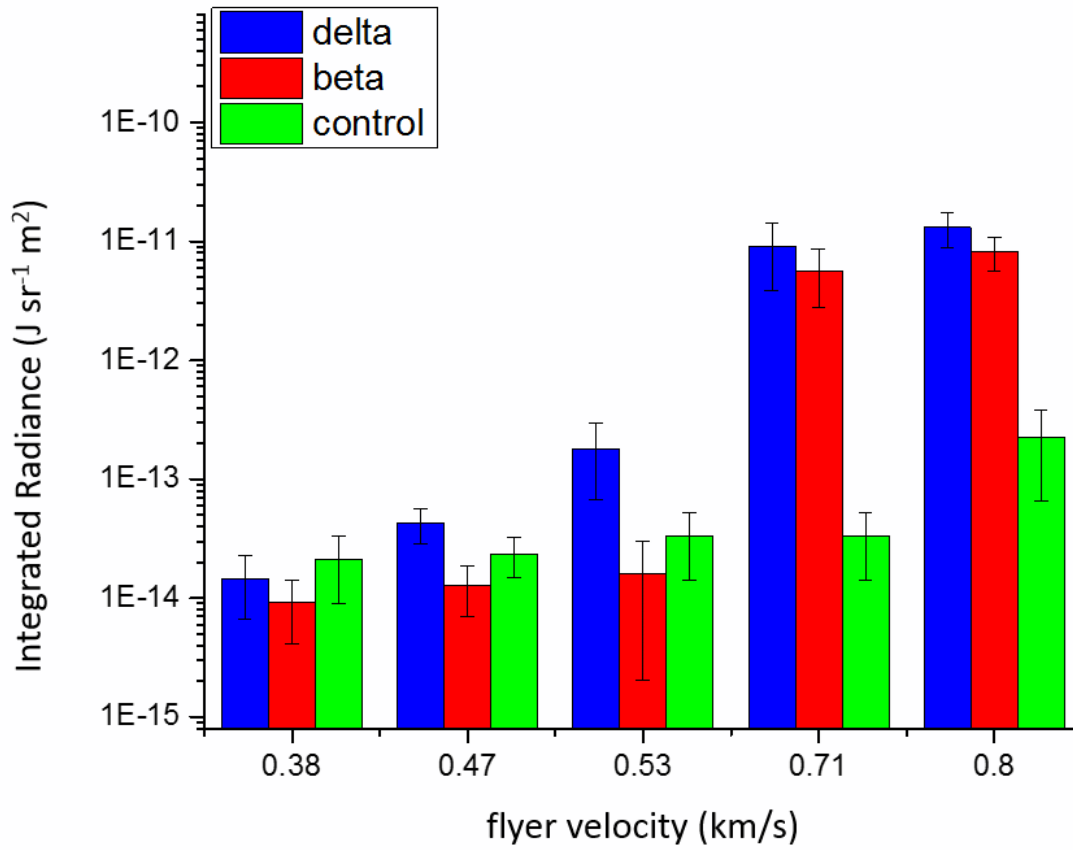
Figure 5.2. Average values and error bars for the radiance integrated over the first 100ns after flyer impact for the listed flyer velocities
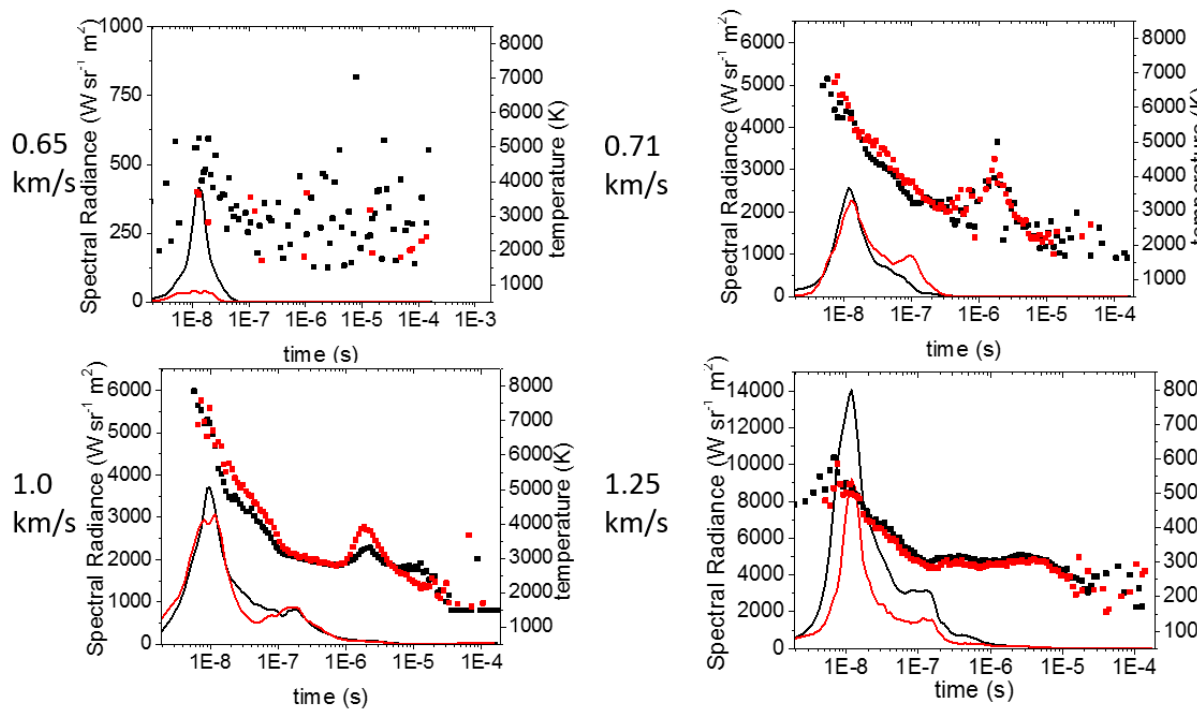
Figure 5.3. Time dependent spectral radiance and temperature from
sprayed δ-HMX (black) and β-HMX (red) at indicated velocities
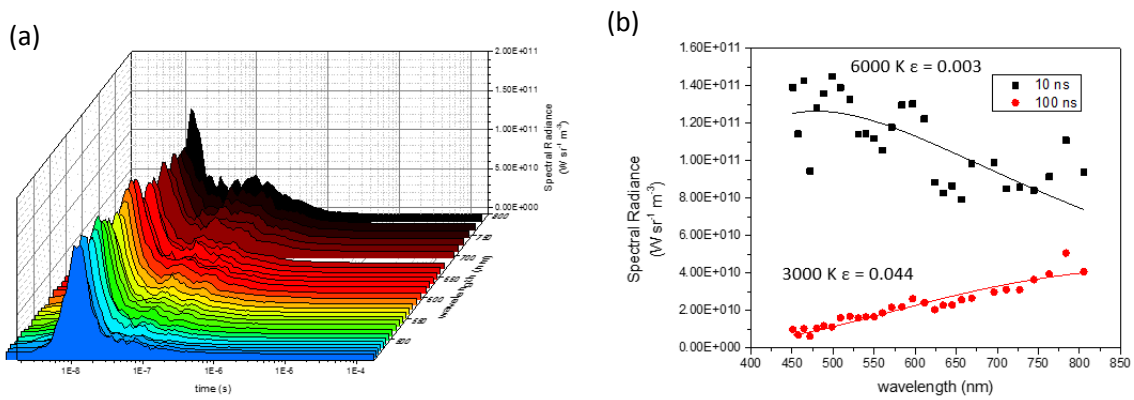
Figure 5.4. (a)Emission spectra from a 1.0 km/s impact on HMX by a 50um flyer plate, showing both a 10 ns burst and a 100 ns burst. (b) Wavelength-resolved spectra radiance during the two burst, with fitted graybody spectrum overlaid